

# REPORT 1116

## APPLICATION OF A CHANNEL DESIGN METHOD TO HIGH-SOLIDITY CASCADES AND TESTS OF AN IMPULSE CASCADE WITH 90° OF TURNING<sup>1</sup>

By JOHN D. STANITZ and LEONARD J. SHELDRAKE

### SUMMARY

*A technique is developed for the application of a channel design method to the design of high-solidity cascades with prescribed velocity distributions as a function of arc length along the blade-element profile. The technique applies to both incompressible and subsonic compressible, nonviscous, irrotational fluid motion. For compressible flow, the ratio of specific heats is assumed equal to  $\gamma = 1.0$ . An impulse cascade with 90° turning was designed for incompressible flow and was tested at the design angle of attack over a range of downstream Mach number from 0.2 to choke flow. To achieve good efficiency, the cascade was designed for prescribed velocities and maximum blade loading according to limitations imposed by considerations of boundary-layer separation.*

### INTRODUCTION

In order to obtain large pressure ratios per stage in axial-flow compressors and turbines, cascades of blade elements with large fluid-turning angles are required. High-solidity blading is required to achieve these large turning angles without serious shock losses due to supersonic peak velocities and without boundary-layer separation due to excessive blade loading. However, because friction losses increase with the ratio of wetted surface to flow area, it is desirable that the blades be as highly loaded as possible so that the solidity be no greater than necessary. Thus it is desirable to have design methods for high-solidity cascades with maximum prescribed velocities that do not result in shock losses and with maximum prescribed deceleration rates that do not result in boundary-layer separation. Such blade elements should have optimum efficiency for the prescribed turning angle of the fluid.

Two types of method are used for the design of blade elements in cascade: (1) airfoil methods, and (2) channel-flow methods. Airfoil methods have been developed for incompressible and linearized compressible flow (refs. 1 to 5, for example). These methods are exact for irrotational, nonviscous fluid motion but generally become difficult to apply if the blade-element solidity is large (1.5 or larger).

For high blade-element solidities, channel-flow methods of design are used, in which the channel between blades is designed and the "islands" between adjacent channels (fig. 1) constitute the blade elements, with the nose and tail of the islands rounded off. Geometric methods for channel design based on the combination of several circular arcs have been used extensively (ref. 6, for example), but these methods have no direct control over the velocity distribution along the blade-element profile.

In reference 7 the shape of the mean streamline between

blade-element profiles and the velocity distribution along this streamline are prescribed together with the blade spacing, and the resulting blade-element profile and velocity distribution along it are determined. The method involves approximations that are accurate for high-solidity cascades, but has no direct control over the velocity distribution along the profile surface.

Design methods for blade elements of high-solidity cascades with prescribed velocities along the blade-element profile are given in references 8 to 10. All these methods involve approximations. In reference 8 the desired velocity distribution is obtained by trial-and-error methods. In reference 9 the shape of one channel wall and the velocity distribution along it are prescribed so that, as in reference 7, the problem is overdetermined and therefore approximate. In reference 10 the manner in which various flow conditions vary across the channel of high-solidity cascades is assumed.

A technique for application of the channel design methods of reference 11 to the design of high-solidity cascades with prescribed velocity distributions as a function of arc length along the blade-element profiles is presented herein. The technique applies to both incompressible and subsonic compressible, nonviscous, irrotational fluid motion. For compressible flow the ratio of specific heats is assumed equal to

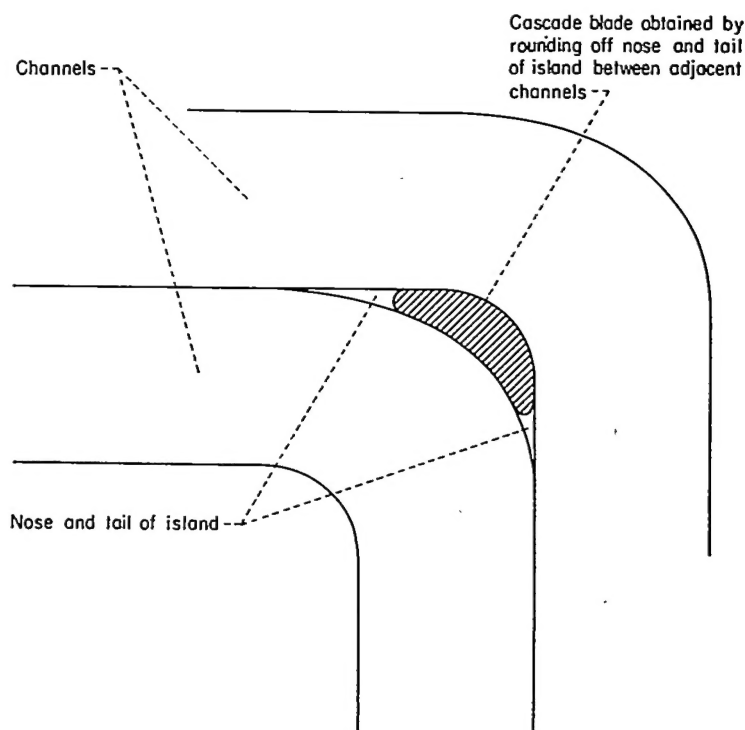


FIGURE 1.—Cascade blade obtained in  $xy$ -plane by rounding off nose and tail of island between adjacent channels designed for prescribed velocity distribution along walls.

<sup>1</sup> Supersedes NACA TN 2652, "Application of a Channel Design Method to High-Solidity Cascades and Tests of an Impulse Cascade With 90° of Turning" by John D. Stanitz and Leonard J. Sheldrake, 1952

—1.0. The design method gives exact results except for the approximation resulting from rounding off the nose and tail of the blade element. In order to investigate the validity of rounding off the nose and tail and to investigate effects of compressibility and viscosity, a high-solidity,  $90^\circ$  impulse cascade was designed and tested. In order to achieve good efficiency, the cascade was designed for prescribed velocities and maximum blade loading according to limitations imposed by boundary-layer separation (ref. 12). The cascade was developed for incompressible flow and was tested at the design angle of attack over a range of downstream Mach number from 0.2 to choke flow. The data were analyzed and correlated by methods developed in the report.

The application of a channel design method to high-solidity cascades reported herein was developed at the NACA Lewis laboratory during 1951 and is part of a doctoral thesis conducted by the senior author with the advice of Professor Ascher H. Shapiro of the Massachusetts Institute of Technology.

### CASCADE DESIGN METHOD

A cascade design method based on the channel design methods of reference 11 is developed for nonviscous, irrotational, incompressible or compressible fluid motion.

#### THEORY OF METHOD

**Outline.**—Consider the flow of fluid past the high-solidity cascade in figure 2. Any two blade elements and their respec-

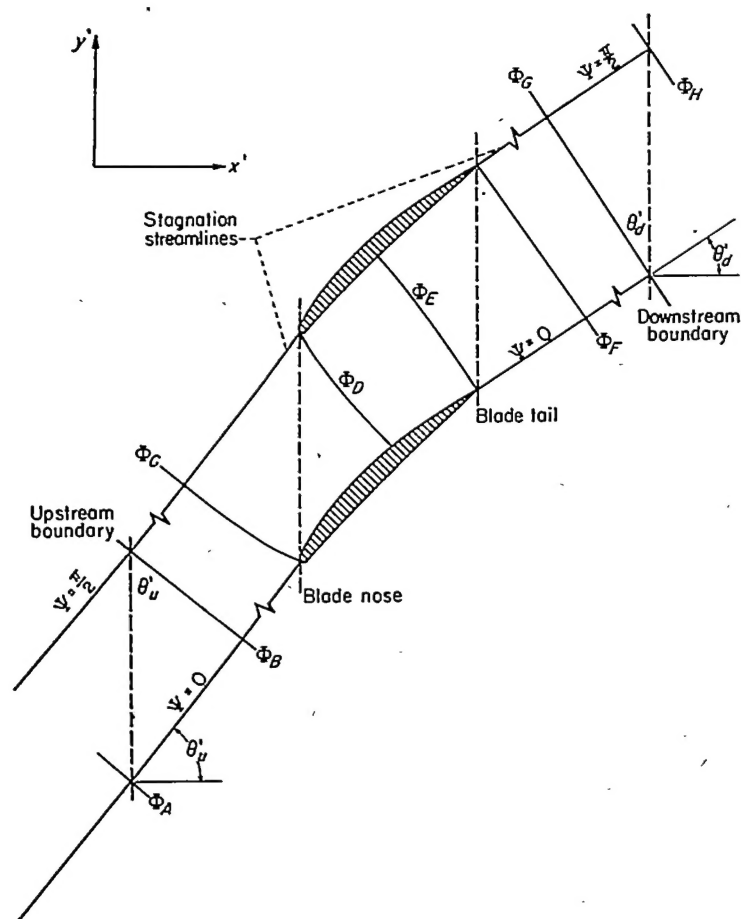


FIGURE 2.—Channel between adjacent stagnation streamlines with velocity potential lines and subscript conventions for flow through cascade.

tive stagnation streamlines upstream and downstream of the cascade constitute a flow channel. In the proposed high-solidity cascade design method the shape of this channel will be determined, except for regions in the vicinity of stagnation points, for prescribed variations in velocity as a function of arc length  $s$  along the channel walls between points corresponding to the nose and tail of the blade elements. The channel design methods of reference 11 will be used to solve for the shape of this channel between high-solidity blade elements.

The flow field of the two-dimensional channel between blade elements is considered to lie in the physical  $xy$ -plane where  $x$  and  $y$  are Cartesian coordinates for which the units are so chosen that the channel width downstream at infinity is unity. (All symbols are defined in appendix A.)

At each point in the channel between blade elements the velocity vector (fig. 3) has a magnitude  $Q$  and a direction  $\theta$ , where  $Q$  is the fluid velocity for which the units are so chosen that the channel velocity downstream at infinity is unity. For compressible flow, the velocity  $q$  is related to the velocity ratio  $Q$  by

$$q = Qq_a$$

where  $q$  is the velocity for which the units are so chosen that the stagnation speed of sound is unity and where the subscript  $a$  refers to conditions downstream at infinity.

Solutions for two-dimensional flow are boundary-value problems. That is, the solutions depend on known conditions imposed along the boundaries of the problem. In the inverse problem of channel design the geometry of the channel walls in the physical plane is unknown. This unknown geometry apparently precludes the possibility of solving the problem in the physical plane and necessitates the use of some

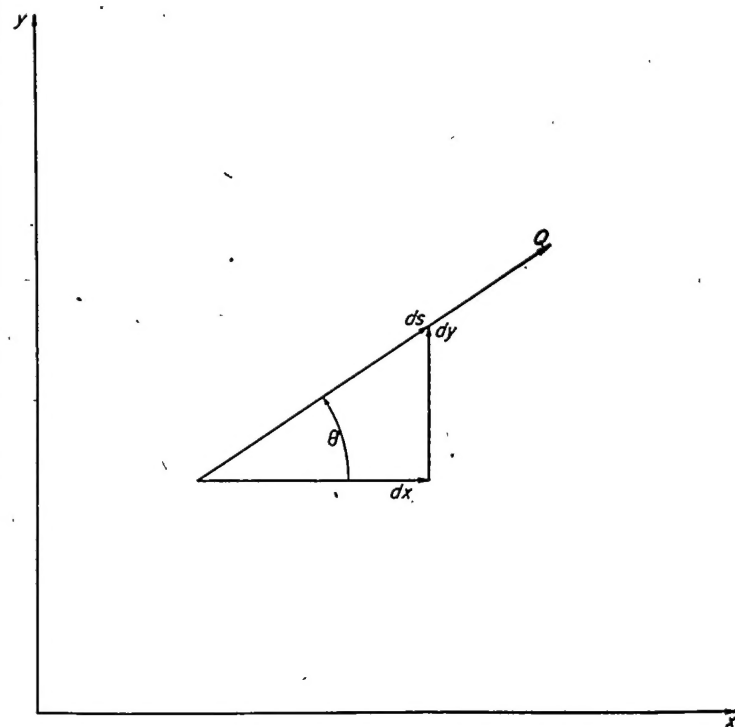


FIGURE 3.—Magnitude and direction of velocity at point in  $xy$ -plane.

new plane. This new plane must be such that the shape of the boundaries along which the velocities are prescribed is known. It is also desirable that the coordinate system of the new plane be orthogonal in the physical plane. A set of coordinates that satisfies these requirements is provided by the velocity potential lines of constant  $\Phi$  and the streamlines of constant  $\Psi$  (where  $\Phi$  and  $\Psi$  are defined in ref. 11), which are orthogonal in the  $xy$ -plane and for which the geometric boundaries are known constant values of  $\Psi$  (equal to 0 and  $\pi/2$ ) in the  $\Phi\Psi$ -plane. The distribution of velocity as a function of  $\Phi$  along these boundaries of constant  $\Psi$  is known because, if

$$Q=Q(s)$$

or

$$q=q(s)$$

is prescribed, the definition of  $\Phi$  (ref. 11) gives

$$\Phi=\Phi(s)$$

from which

$$Q=Q(\Phi)$$

or

$$q=q(\Phi)$$

The technique of the channel design methods developed in reference 11 is therefore to solve for the physical  $xy$ -coordinates of the channel walls in the  $\Phi\Psi$ -plane where the prescribed boundary conditions for the two-dimensional flow problem are known.

The channel design methods of reference 11 are applied to the design of high-solidity cascades as follows: Along the upstream and downstream stagnation streamlines (fig. 2) the velocity will be assumed constant and equal to the upstream and downstream velocities, respectively. The stagnation points on the blade surface are ignored (which practice results in a cusped nose and tail that are rounded off, as indicated previously), and the velocity at the nose and tail are assumed equal to the upstream and downstream velocities, respectively. Along the channel wall corresponding to the suction surface of the blade element, the velocity accelerates from its upstream value at the nose to some maximum value, after which it decelerates to its downstream value at the tail. Along the channel wall corresponding to the pressure surface of the blade element, the velocity decelerates from its upstream value at the blade nose to some minimum value, after which it accelerates to the downstream value at the tail.

Because of the velocity difference over that portion of the channel walls corresponding to the blade-element surfaces, the channel turns the fluid an amount  $\Delta\theta$  that can be computed by equation (H5) of reference 11. If a specified value of  $\Delta\theta$  is desired, the prescribed velocity distribution must be adjusted, by methods to be considered later, to obtain this turning.

The physical coordinates of the channel are determined in the  $\Phi\Psi$ -plane for the prescribed velocity distribution according to the design methods of reference 11. The islands between adjacent channels (fig. 1) in the physical  $xy$ -plane constitute the blade-element profiles. The cusped nose and tail of these islands are rounded off at the previously selected positions for the nose and tail of the blade-element profiles.

**Nose and tail positions in  $\Phi\Psi$ -plane.**—Because the channel

design is carried out in the  $\Phi\Psi$ -plane, it is necessary to determine the positions of the nose and tail on the pressure and suction surfaces of the channel walls in the  $\Phi\Psi$ -plane. Consider the flow of fluid corresponding to the channel between blades (fig. 2). The change in velocity potential  $\Phi$  from the upstream boundary, at which conditions are considered uniform, to the nose must be equal along both upstream stagnation streamlines so that

$$\Phi_C - \Phi_A = \Phi_D - \Phi_B$$

from which

$$\Phi_D - \Phi_C = \Phi_B - \Phi_A \quad (1)$$

where the subscripts  $A, B, C, D$ , and so forth, refer to positions defined by the velocity potential lines in figure 2. But, because conditions are uniform along the upstream boundary,

$$\frac{\Phi_B - \Phi_A}{\pi/2} = \tan \theta'_u \quad (2)$$

where  $\pi/2$  is the change in  $\Psi$  across the channel and where the angle  $\theta'$  is measured counterclockwise from the positive  $x'$ -axis of the  $x', y'$ -coordinate system in which the cascade lies along the  $y'$ -axis. From equations (1) and (2)

$$\Phi_D - \Phi_C = \frac{\pi}{2} \tan \theta'_u \quad (3)$$

Equation (3) determines the difference in  $\Phi$  on the two walls of the channel at the points in the  $\Phi\Psi$ -plane corresponding to the nose of the cascade blade. Likewise, the difference in  $\Phi$  on the two walls of the channel at the points in the  $\Phi\Psi$ -plane corresponding to the tail of the cascade blade is given by

$$\Phi_F - \Phi_E = \frac{\pi}{2} \tan \theta'_d \quad (4)$$

Equations (3) and (4) determine the relative positions on the channel walls in the  $\Phi\Psi$ -plane of points corresponding to the nose and tail of the blade profile, respectively.

**Prescribed velocity distribution.**—In general, the prescribed distribution of velocity as a function of arc length along the channel walls between blade-element profiles can be arbitrary for the proposed blade-element design method except that the velocity is higher on the suction surface than on the pressure surface, the resulting blade-element profile must be practical, and the difference in velocity distribution on the two walls must satisfy equations (3) and (4). In addition, the prescribed velocity distribution must result in the prescribed turning angle. This last condition can be determined by computing the turning angle from equation (H5) of reference 11 and, in general, the original velocity distribution must be adjusted by trial-and-error methods to achieve the correct (prescribed) turning angle. Along the channel walls upstream and downstream of the points (and at the points) corresponding to the nose and tail of the blade-element profile (fig. 2), the velocity is assumed constant and equal to the upstream and downstream velocities, respectively.

In the remainder of this report it is assumed that the velocity distribution is prescribed, for convenience, by  $\log Q$  (for incompressible flow) as a linear function of  $\Phi$

along the channel walls in the  $\Phi\Psi$ -plane. A typical example of such a velocity distribution is given in figure 4. The velocity accelerates along the suction surface ( $\Psi=0$ ) from the upstream value  $Q_u$  at the nose  $\Phi_C$  to a maximum value  $Q_{max}$  at which it remains constant until it decelerates to the downstream value  $Q_d$  at the tail  $\Phi_E$ . The velocity decelerates along the pressure surface ( $\Psi=\pi/2$ ) from the upstream value  $Q_u$  at the nose  $\Phi_D$  to a minimum value  $Q_{min}$  at which it remains constant until it accelerates to the downstream value  $Q_d$  at the tail  $\Phi_F$ . The accelerating flow along the suction surface and the decelerating flow along the pressure surface near the blade nose and vice versa near the tail will, in general, result in a physically practical blade-element profile. An equation for the turning angle  $\Delta\theta$  that results from this linear distribution of  $\log_e Q$  and which must satisfy the prescribed turning angle is developed next.

**Turning angle  $\Delta\theta$ .**—From appendix H of reference 11 the channel or cascade turning angle  $\Delta\theta$  is given by (for incompressible flow)

$$\Delta\theta = \frac{-2}{\pi} \int_{-\infty}^{\infty} \Phi \left[ \left( \frac{\partial \log_e Q}{\partial \Phi} \right)_{\frac{\pi}{2}} - \left( \frac{\partial \log_e Q}{\partial \Phi} \right)_0 \right] d\Phi \quad (5)$$

For linear variations in  $\log_e Q$  with  $\Phi$

$$\frac{\partial \log_e Q}{\partial \Phi} = \frac{\Delta \log_e Q}{\Delta \Phi} = \text{constant}$$

and for the type of linear velocity distribution given in figure 4, equation (5) integrates to give

$$\Delta\theta = \frac{1}{\pi} \left[ \left( \log_e \frac{Q_{max}}{Q_u} \right) (\Phi_C + \Phi_{CC}) + \left( \log_e \frac{Q_d}{Q_{max}} \right) (\Phi_{EE} + \Phi_E) - \left( \log_e \frac{Q_{min}}{Q_u} \right) (\Phi_D + \Phi_{DD}) - \left( \log_e \frac{Q_d}{Q_{min}} \right) (\Phi_{FF} + \Phi_F) \right] \quad (6)$$

which is the cascade turning angle. For a prescribed value of  $\Delta\theta$ , equation (6) establishes a relation among  $Q_{max}$ ,  $Q_{min}$ ,  $Q_u$ ,  $Q_d$ ,  $\Phi_C$ ,  $\Phi_{CC}$ ,  $\Phi_D$ ,  $\Phi_{DD}$ ,  $\Phi_E$ ,  $\Phi_{EE}$ ,  $\Phi_F$ , and  $\Phi_{FF}$ . For linearized compressible flow, linear distributions of  $\log_e V$  (defined in ref. 11) with  $\Phi$  of the type shown in figure 4 could be prescribed, in which case the turning angle  $\Delta\theta$  would be given by equation (6) with  $Q$  replaced by  $V$ .

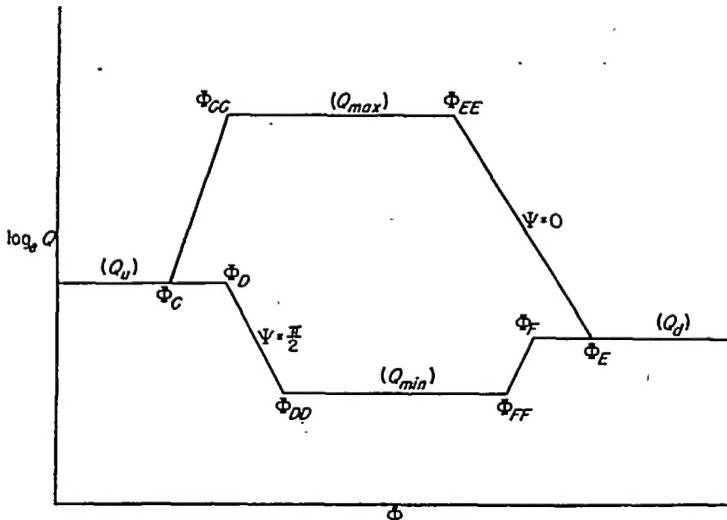


FIGURE 4.—Typical example of linear, prescribed variation in  $\log_e Q$  with  $\Phi$ , including subscript convention for  $\Phi$  and  $Q$ .

**Allowable deceleration on suction surface.**—In order to achieve the desired turning  $\Delta\theta$  with the minimum number of blades, the difference ( $Q_{max} - Q_{min}$ ) for incompressible flow or ( $V_{max} - V_{min}$ ) for compressible flow must be large; and the arc length over which  $Q_{max}$  and  $Q_{min}$  are prescribed should be extensive. However, the magnitude of  $Q_{max}$  is limited by shock losses (compressible flow) and cavitation (incompressible flow). Also, the arc length over which  $Q_{max}$  is prescribed is limited (in percentage of total suction surface length) by the allowable rate of deceleration from  $Q_{max}$  to  $Q_d$  along the suction surface near the blade tail. This limitation will be considered next. The deceleration from  $Q_u$  to  $Q_{min}$  along the pressure surface near the blade nose is not so critical because the boundary layer is thin in this region.

The allowable deceleration without boundary-layer separation on the suction surface is determined by the ratio  $Q_d/Q_{max}$  and the blade-element Reynolds number based on blade chord (ref. 12). This allowable deceleration can be expressed as a ratio  $\lambda$  of arc lengths, where  $\lambda$  is defined by

$$\lambda = \frac{s_{EE} - s_C}{s_E - s_C} \quad (7)$$

where the reference point for  $s$  is arbitrary. The maximum allowable value of  $\lambda$  for given values of  $Q_d/Q_{max}$  and Reynolds number is given in reference 12.

From equations (4), (16), and (40) of reference 11 the arc length ( $s_{EE} - s_C$ ) is given by

$$\frac{\pi}{2} (s_{EE} - s_C) = \int_{\Phi_C}^{\Phi_{CC}} \frac{d\Phi}{Q} + \int_{\Phi_{CC}}^{\Phi_{EE}} \frac{d\Phi}{Q} \quad (8)$$

where for the type of velocity distribution in figure 4

$$\left. \begin{aligned} \log_e Q &= \log_e Q_u + (\log_e Q_{max} - \log_e Q_u) \left( \frac{\Phi - \Phi_C}{\Phi_{CC} - \Phi_C} \right) & (\Phi_C \leq \Phi \leq \Phi_{CC}) \\ \log_e Q &= \log_e Q_{max} & (\Phi_{CC} \leq \Phi \leq \Phi_{EE}) \end{aligned} \right\} \quad (9)$$

From equations (8) and (9)

$$\frac{\pi}{2} (s_{EE} - s_C) = \frac{\Phi_{CC} - \Phi_C}{\log_e \frac{Q_{max}}{Q_u}} \left( \frac{Q_{max} - Q_u}{Q_{max} Q_u} \right) + \frac{\Phi_{EE} - \Phi_{CC}}{Q_{max}}$$

and, likewise,

$$\frac{\pi}{2} (s_E - s_C) = \frac{\pi}{2} (s_{EE} - s_C) + \frac{\Phi_E - \Phi_{EE}}{\log_e \frac{Q_d}{Q_{max}}} \left( \frac{Q_d - Q_{max}}{Q_d Q_{max}} \right)$$

so that equation (7) becomes

$$\Phi_E = \Phi_{EE} + \frac{1 - \lambda}{\lambda} \left[ \frac{\Phi_{CC} - \Phi_C}{\log_e \frac{Q_{max}}{Q_u}} \left( \frac{Q_{max} - Q_u}{Q_u} \right) + \frac{\Phi_E - \Phi_{CC}}{Q_d - Q_{max}} \right] \frac{Q_d \log_e \left( \frac{Q_d}{Q_{max}} \right)}{Q_d - Q_{max}} \quad (10)$$

Equation (10) determines the minimum value for  $\Phi_E$  if the maximum allowable rate of deceleration between  $\Phi_{EE}$  and  $\Phi_E$  is not to be exceeded.



The values for  $\lambda$  in reference 12 are based on maximum allowable safe rates of deceleration which decrease in the direction of flow as the boundary-layer thickness increases. Thus the required distribution of  $\log_e Q$  along  $\Phi$  is not necessarily linear as assumed in this report. However, as will be shown in the section Prescribed velocity distribution, the assumed distribution of  $\log_e Q$  with  $\Phi$  has similar characteristics to those required in reference 12 and is considered accurate enough for engineering purposes.

**Rounding off nose and tail of blade-element profile.**—After the prescribed velocity distribution has been selected to meet the conditions discussed previously, the channel shape is determined by the numerical methods developed in reference 11. The islands between adjacent channels (fig. 1) in the physical  $xy$ -plane constitute the blade-element profiles. Because the stagnation points are not considered in this design method, the nose and tail of the blade element are cusped. These cusps are eliminated by faired curves (circular arcs, for example) that are tangent to the channel walls at the previously selected positions for the nose and tail of the blade-element profiles.

#### DESIGN PROCEDURE

The various conditions to be satisfied in the application of the channel design method to the design of high-solidity cascades of blades with prescribed velocity distributions along the blade contours have been discussed, and the details of the numerical procedure for the channel design itself are the same as those outlined in reference 11. A brief step-by-step outline of the conditions to be satisfied and the numerical procedure follows:

(1) The cascade, or channel, turning angle  $\Delta\theta$  and the upstream and downstream velocities  $q_u$  and  $q_d$  are prescribed. (For incompressible flow the upstream velocity  $Q_u$  is sufficient because  $Q_d$  equals 1.0.) The cascade stagger angle is fixed by these prescribed conditions and the equation of continuity. The flow may be incompressible or compressible ( $\gamma$  equal to  $-1.0$ ).

(2) The solution for the equivalent channel wall coordinates will be carried out in the  $\Phi\Psi$ -plane. The relative positions of points on the channel walls in the  $\Phi\Psi$ -plane,  $(\Phi_D - \Phi_C)$  and  $(\Phi_F - \Phi_E)$  in figure 2, corresponding to the nose and tail of the blade profile are determined by equations (3) and (4).

(3) The prescribed velocity along the channel walls upstream of  $\Phi_C$  and  $\Phi_D$  is equal to the upstream velocity.

(4) The prescribed velocity along the channel walls downstream of  $\Phi_E$  and  $\Phi_F$  is equal to the downstream velocity.

(5) The velocity distribution along the suction surface of the blade-element profile, between the points  $\Phi_C$  and  $\Phi_E$  (fig. 2) on the channel wall in the transformed  $\Phi\Psi$ -plane, is prescribed as an arbitrary function of arc length. Usually a practical blade shape results if the prescribed velocity increases from the upstream value at the nose ( $\Phi_C$ ) and then decreases to the downstream value at the tail ( $\Phi_E$ ).

(6) The prescribed velocity along the pressure surface of the blade-element profile, between the points  $\Phi_D$  and  $\Phi_F$  (fig. 2) on the channel wall in the transformed  $\Phi\Psi$ -plane, is

prescribed as an arbitrary function of arc length along the blade profile. Usually a practical blade shape results if the prescribed velocity decreases from the upstream value at the nose ( $\Phi_D$ ) and then increases to the downstream value at the tail ( $\Phi_F$ ).

(7) In order to obtain an efficient high-solidity cascade, the difference in prescribed velocities on the channel walls corresponding to the suction and pressure surfaces of the blades should be large so that the blade spacing is large enough to prevent serious friction losses. But the maximum prescribed velocity on the suction surface should not be so large that losses result from shock or that serious boundary-layer separation losses result from rapid deceleration to the downstream velocity at the blade tail ( $\Phi_E$  in fig. 2).

(8) The prescribed velocity distribution on the channel walls must satisfy the prescribed cascade, or channel, turning angle  $\Delta\theta$ . This angle is determined by equation (H5) of reference 11. If the prescribed velocity distribution does not satisfy the prescribed turning angle, the velocity distribution is adjusted by trial-and-error methods; or, for the type of linear velocity distributions given in figure 4, the proper adjustment in velocity can be determined directly from equation (6).

(9) After the prescribed velocity distribution that satisfies the conditions just outlined has been selected, the channel design is determined by methods outlined in reference 11.

(10) The cusped nose and tail of the islands that result between adjacent channels in the physical plane (fig. 1) are rounded off by faired curves (circular arcs, for example) that are tangent to the channel walls at points corresponding to the nose and tail of the blade element ( $\Phi_C$  through  $\Phi_F$  in fig. 2). Finally, if desired, the displacement thickness of the boundary layer can be estimated by boundary-layer theory and subtracted from the preceding contours to obtain the final blade profile. Thus the high-solidity cascade design is complete.

#### NUMERICAL EXAMPLE

In general, as the percentage reaction decreases and as the blade camber (or turning angle) increases, the cascade efficiency decreases (ref. 13, p. 232). The problem selected is therefore to design an efficient impulse cascade (zero percent reaction) with large turning angle.

**Prescribed conditions.**—An impulse cascade with  $90^\circ$  of turning was designed for incompressible flow with the following prescribed conditions:

$$\left. \begin{aligned} (1) \theta'_u &= \pi/4 \\ (2) \theta'_d &= -\pi/4 \end{aligned} \right\} \Delta\theta = \frac{\pi}{2} = 90^\circ$$

$$(3) Q_u = Q_d = 1.0$$

**Prescribed velocity distribution.**—For convenience the velocity distribution has been specified by linear variations in  $\log_e Q$  with  $\Phi$ . The following conditions were arbitrarily selected:

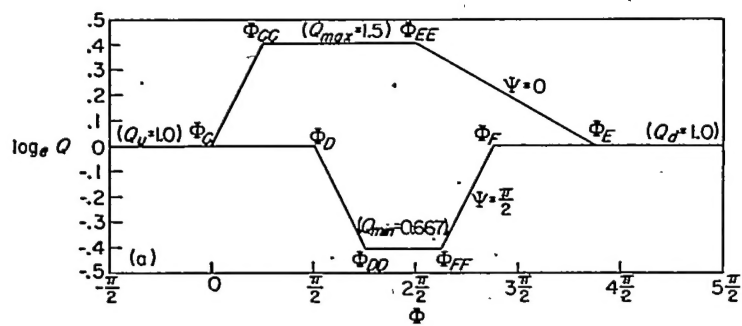
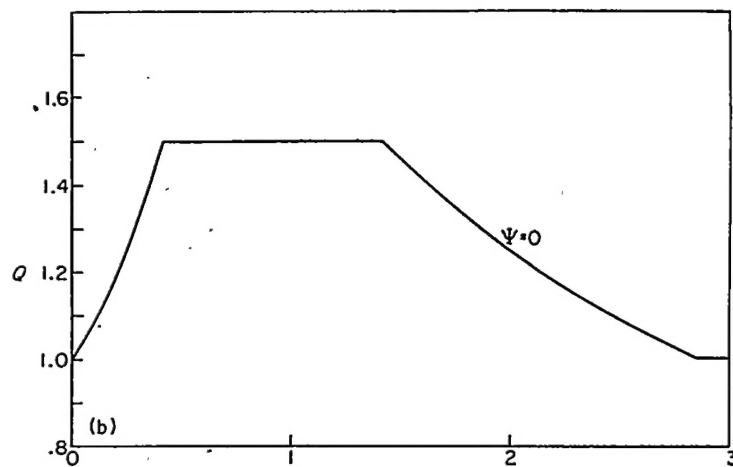
$$(1) Q_{max} = 1.5$$

$$(2) \Phi_C = 0$$

$$(3) \Phi_{CC} - \Phi_C = \Phi_{DD} - \Phi_D = \Phi_F - \Phi_{FF} = \frac{\pi}{4}$$

$$(4) \Phi_{EE} = \pi$$

The quantities  $(\Phi_D - \Phi_C)$  and  $(\Phi_F - \Phi_E)$  are obtained from equations (3) and (4) and are equal to  $\pi/2$  and  $-\pi/2$ , re-

(a) Variation in  $\log_e Q$  with  $\phi$ .

(b) Velocity as function of arc length along suction surface.

Figure 5.—Prescribed velocity distribution for 90° impulse cascade blade.

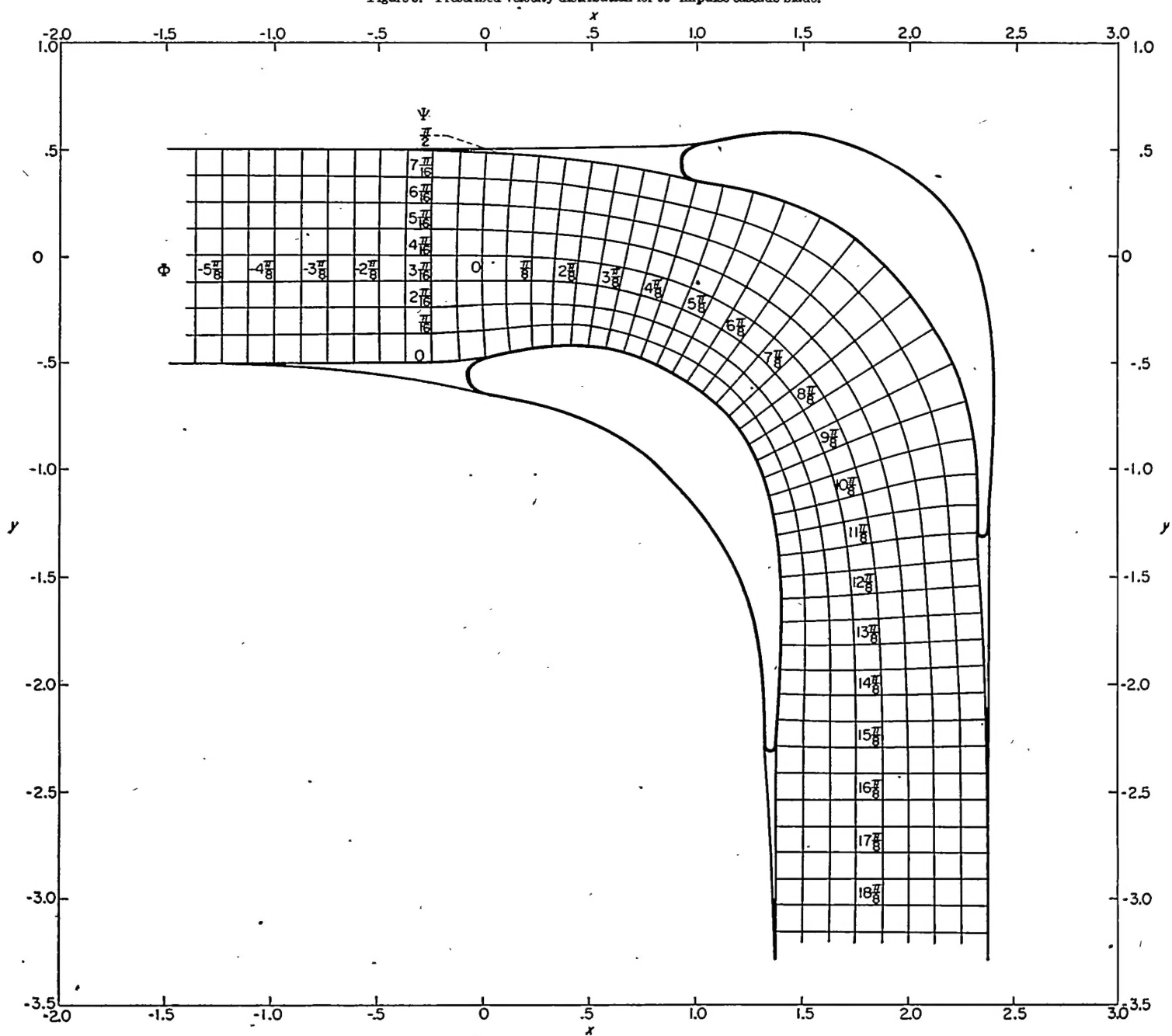


FIGURE 6.—Streamlines and velocity-potential lines for channel between blade elements of 90° impulse cascade. Designed for prescribed velocity distribution given in figure 5 (a).

spectively. The quantity  $\Phi_{\mathbf{x}}$  (fig. 2) is given by equation (10) with  $\lambda$  equal to 0.5, and is equal to  $3.75 \pi/2$ . (The value of 0.5 for  $\lambda$  was obtained from fig. 5 (a) of ref. 12 for  $Q_d/Q_{max}$  equal to 0.667 and for a blade Reynolds number equal to  $\infty$ , which Reynolds number gives the minimum, and therefore safest, value of  $\lambda$ .) The value of  $Q_{min}$  was obtained from equation (6) with  $\Delta\theta$  equal to  $\pi/2$ :

$$Q_{min}=0.66687$$

The resulting prescribed distribution of  $\log_e Q$  with  $\Phi$  is given in figure 5 (a). The corresponding distribution of  $Q$  with arc length  $s$  along the suction surface can be obtained from the definition of  $\Phi$  in reference 11 and is given in figure 5 (b). The velocity distribution between  $Q_{max}$  (1.5) and  $Q_a$  (1.0) is similar in shape to that resulting from the maximum allowable safe rates of deceleration in reference 12, so that the assumed linear variation in  $\log_e Q$  with  $\Phi$  satisfies approximately the conditions on which the results of reference 12 are based.

**Cascade design.**—The channel shape corresponding to the prescribed velocity distribution in figure 5 (a) was determined by the relaxation methods used in reference 11 and is plotted in figure 6 together with the resulting high-solidity cascade of blades formed by rounding off the cusped nose and tail of the islands formed between adjacent channels. For the experimental investigation, a cascade of these blades with a chord of 5.5 inches was constructed, and the coordinates for this blade profile are given in table I. The blade profile was not adjusted to provide for the displacement thickness of the boundary layer. The characteristics of the resulting cascade are given in figure 7 on the  $x'y'$ -plane in which all linear distances are dimensionless, being divided by the blade chord  $c$ . The reciprocal  $s'/c$  of the cascade solidity (where  $s'$  is the blade spacing) is 0.6130. The maximum blade thickness is approximately 18 percent of the chord, the trailing-edge thickness is approximately 2.8 percent of the chord, and the

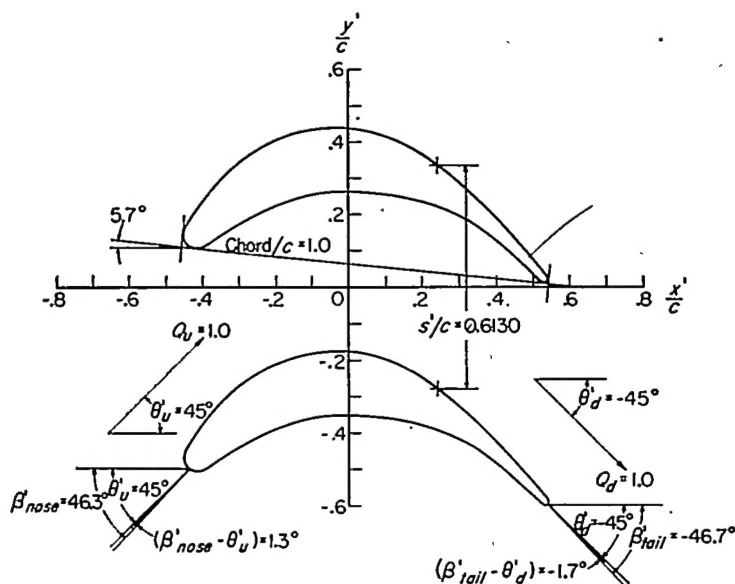


FIGURE 7.— Characteristics of 90° impulse cascade in  $x'y'$ -plane. Coordinates of blade-element profile are given in table I.

radius of the circular arc at the blade nose is 3.7 percent of the blade chord. The average angle  $\beta'_{nose}$  of the blade surfaces tangent to the circular arc at the blade nose is  $46.3^\circ$  so that the blade is overturned  $1.3^\circ$  at the nose (fig. 7). The average angle  $\beta'_{tail}$  of the blade surfaces tangent to the circular arc at the blade tail is  $-46.7^\circ$  so that the blade is overturned  $1.7^\circ$  at the tail. The blade profile is similar in appearance to the best shape developed in reference 6 by combination of circular arcs.

## CASCADE TESTS

An experimental investigation was made on the blade profile just designed in order to determine if rounding off the cusped nose and tail has a serious effect on the resulting agreement between the prescribed velocity distribution on the blade surface and the distribution measured by test and to determine if the design procedure taking into account present knowledge of boundary-layer separation results in efficient blade shapes. In addition, the blade profile, which was designed for incompressible flow, was tested over a range of downstream Mach number from 0.2 to choke flow in order to determine effects of compressibility.

### DESCRIPTION OF APPARATUS

**Flow tank.**—As indicated in the line drawing of figure 8, the cascade of 90° impulse blades was attached to a short tunnel of straight parallel walls that was mounted on a rounded approach at the flow test tank. Dimensions of the tank and piping are given in figure 8. The tank contained a honeycomb of square cells (2 by 2 in.) 8 inches deep. Immediately upstream of the honeycomb were three screens; one 28×30 mesh and two 40×60 mesh with the mesh oriented 90° apart. The tank pressure, and therefore the flow rate, was controlled by a valve upstream of the tank. The maximum flow rate through the tank during the tests was 88

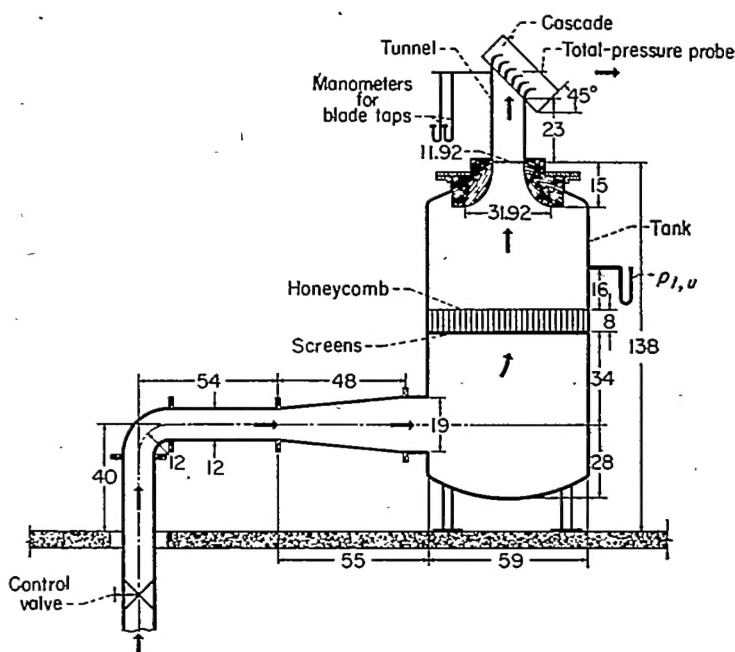


FIGURE 8.—Line drawing of test setup. All linear dimensions in inches.

pounds per second. The rounded approach to the tunnel had an elliptical profile. A photograph of the test setup is shown in figure 9.

**Tunnel.**—The tunnel consisted of straight parallel walls that could not be adjusted to account for boundary-layer growth or to simulate the shape of the stagnation streamlines upstream of the cascade. (For high-solidity cascades the position and shape of the upstream tunnel walls have little effect on flow conditions in the channel between blades where the character of the flow is almost exclusively influenced by the shape of the blades.) The tunnel length was short to prevent large boundary-layer growth on the tunnel walls. The cross section of the tunnel normal to the direction of flow was 11.91 by 16.50 inches.

**Cascade.**—The blade-element profile is described in table I, and the cascade characteristics are given in figure 7. Six blades with a chord of 5.5 inches and an aspect ratio of 3.0 were used (see ref. 14, p. 3). The blade span was therefore 16.5 inches. Based on a blade chord of 5.5 inches, the Reynolds number  $Re$  was approximately related to the downstream Mach number  $M_a$  by

$$Re \approx 3 \times 10^6 M_a$$

Thus for the minimum test value of  $M_a$  equal to 0.2 the Reynolds number was 600,000, which is well above the critical values indicated in reference 12. A photograph of the assembled cascade is shown in figure 10.

#### INSTRUMENTATION

**Tank and tunnel.**—The total pressure upstream of the cascade was measured by a static tap downstream of the honeycomb in the tank (fig. 8). The total temperature of the air was measured by a thermocouple in the tank. Static pressure was measured on the center line of the tunnel walls, 12 inches upstream of the cascade.

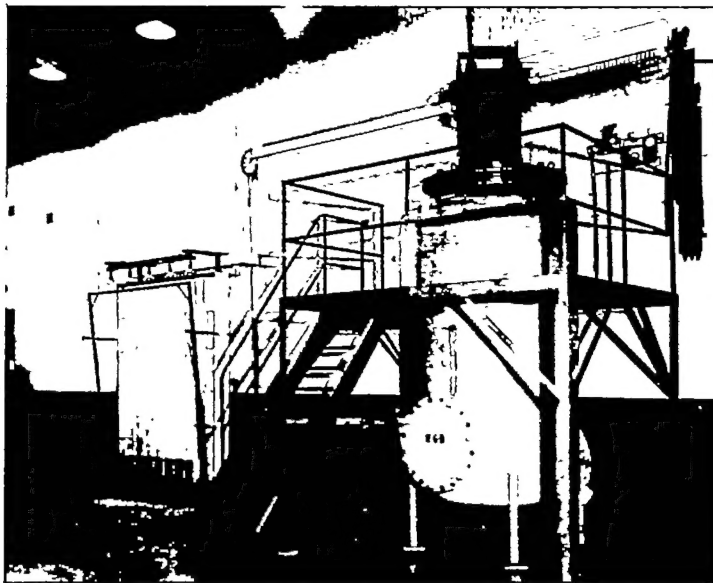


FIGURE 9.—Photograph of test setup.

**Cascade.**—Static pressures at midspan on the blade surfaces of the center channel in the cascade were measured at 48 locations indicated in table II. In addition total-pressure and flow-direction surveys were made at midspan across the center channel between blades in a plane  $1\frac{1}{2}$  inches downstream of the exit plane of the cascade. (The flow direction was essentially constant in the survey plane.) The total-pressure probe was unshielded and the yaw probe was of the wedge type. The static pressure  $p_a$ , used to determine flow conditions downstream of the cascade, was measured at a wall tap located approximately  $1\frac{1}{2}$  inches downstream of the exit plane of the cascade and was for all values of  $M_a$  approximately equal to atmospheric room pressure.

#### TEST RESULTS

Static pressures on the blade surfaces of the center channel in the cascade were obtained for eight values of the downstream Mach number between 0.2 and 0.79. (The cascade choked at a downstream Mach number between 0.75 and 0.79.) In addition, total-pressure surveys were made and the flow direction was measured downstream of the cascade for five values of the downstream Mach number between 0.3 and 0.7. The results are plotted in figures 11 to 14.

**Pressure coefficient  $P$ .**—The pressure coefficient  $P$  is plotted in figure 11 as a function of the coordinate  $x'/c$  along the blade surface (fig. 7). The pressure coefficient  $P$  is defined by

$$P = \frac{p - p_a}{p_{t,a} - p_a} \quad (11)$$

where  $p$  is the static pressure and  $p_{t,a}$  is the total pressure downstream of the cascade exclusive of the wake and is therefore equal to the upstream total pressure. For incompressible flow the pressure coefficient  $P$ , defined by equation (11),

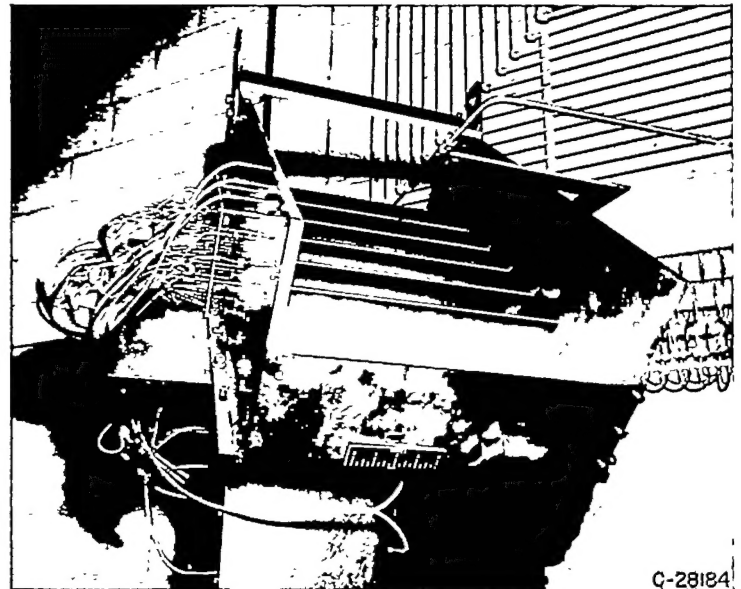


FIGURE 10.—Photograph of cascade with downstream total-pressure probe in position.



reduces to the usual definition for pressure coefficient, that is, pressure difference divided by downstream, or upstream, velocity head. The pressure tap corresponding to a given data point can be determined from the value of  $x'/c$  and table II. For incompressible flow  $P$  is related to  $Q$  by

$$P = 1 - Q^2$$

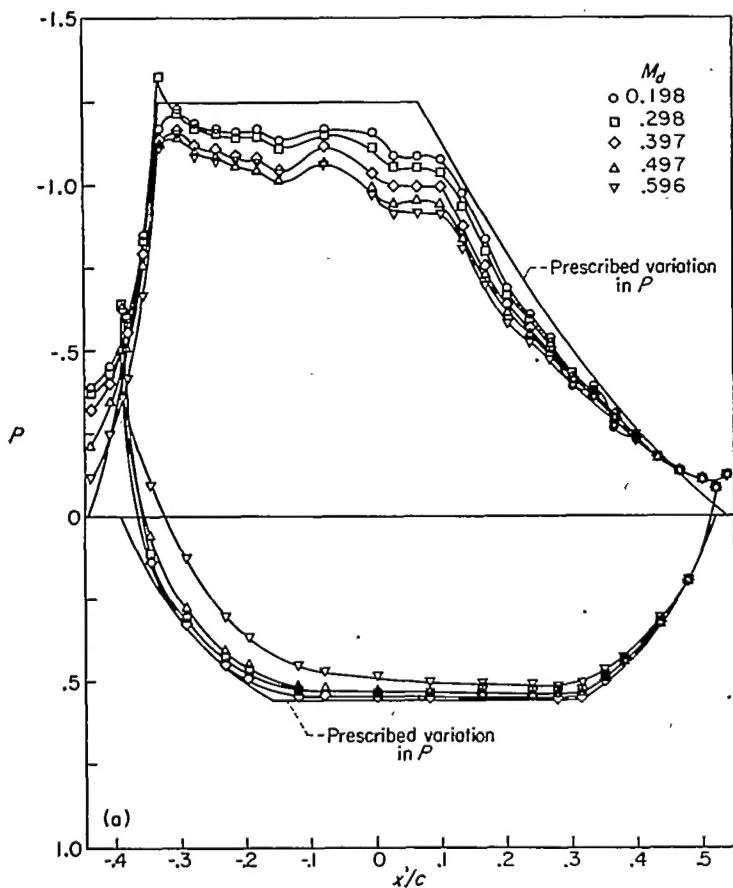
The variation in  $P$  with  $x'/c$  for the design variation in  $Q$  is given by the regular solid lines in figure 11.

In figure 11 (a) the results are plotted for the downstream Mach numbers between 0.2 and 0.6. For these Mach numbers the flow is everywhere subsonic. The agreement between the measured and prescribed (design) values of  $P$  is good for  $M_d$  equal to 0.198, but becomes progressively worse because of compressibility effects as  $M_d$  increases. In general, the discrepancy between the measured and prescribed values of  $P$  at  $M_d$  equal to 0.198 can be attributed in part to the lower-than-design flow rate that results from the reduced effective flow area due to the wake displacement downstream of the cascade. That is, the channel between blades turned a slightly smaller quantity of fluid than designed for, and therefore required slightly less pressure difference on the blade surfaces. The important discrepancy between the

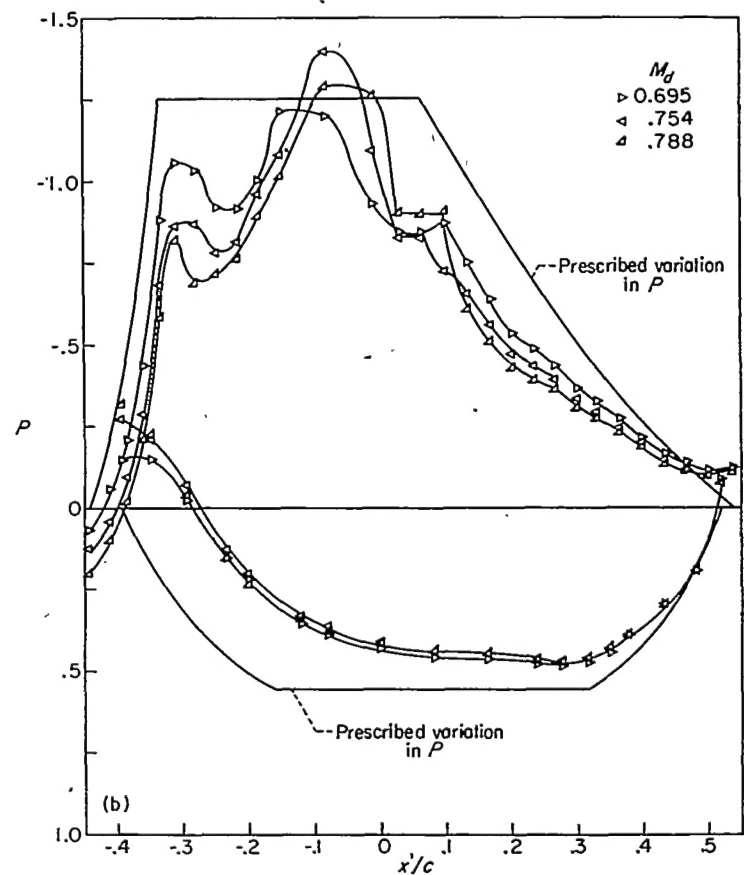
design and experimental value of  $P$  on the pressure surface at the nose ( $x'/c$  equal to  $-0.393$ ) results from rounding off the blade nose and will be discussed later.

In figure 11 (b) the results ( $P$  against  $x'/c$ ) are plotted for downstream Mach numbers of 0.70, 0.75, and 0.79. For these Mach numbers it will be shown that local regions of supersonic flow exist on the suction surface of the blade and shock phenomena result as indicated by the rapid fluctuation in pressure. For all three of these values of downstream Mach number two regions of shock appear on the suction surface; one at  $x'/c$  approximately equal to  $-0.275$  and the other centrally located around  $x'/c$  equal to zero.

**Velocity  $Q$ .**—The velocity  $Q$ , which is dimensionless, having been divided by the downstream velocity, is plotted in figure 12 as a function of the ideal (design) velocity potential  $\Phi$  along the blade surface. The pressure tap corresponding to a given data point can be determined from the value of  $\Phi$  and table II. The prescribed variation in  $Q$  with  $\Phi$  is given by the regular solid lines in figure 12. The experimental values of  $Q$  were obtained from the total pressure and the measured static pressures. The total pressure was assumed equal to the tank pressure, so that in the presence of shock losses the computed velocities are indicative only.



(a) Downstream Mach numbers between 0.2 and 0.6.



(b) Downstream Mach numbers of 0.70, 0.75, and 0.79.

FIGURE 11 — Variation in test values of pressure coefficient  $P$  with position  $x'/c$  along surface of blade element. (The pressure tap corresponding to a given data point can be determined from the value of  $x'/c$  and table II.)

In figure 12 (a) the variation of velocity  $Q$  with  $\Phi$  is plotted for the downstream Mach numbers between 0.2 and 0.6. For these Mach numbers the flow is everywhere subsonic, and the agreement with the prescribed velocity distribution is considered quite good and appears to be independent of the downstream Mach number  $M_d$ . (This independence of downstream Mach number will be discussed in the section Compressibility effects.) It is concluded that blades for high-solidity cascades can be designed for prescribed velocities by the channel flow methods of this report and that rounding off the nose and tail of the blade-element profile has negligible effect on the velocity distribution along the blade surface except in the vicinity of the blade nose. The discrepancy at the blade nose will be discussed in the section Continuity.

In figure 12 (b) the variation in velocity  $Q$  with  $\Phi$  is plotted for downstream Mach numbers of 0.70, 0.75, and 0.79. For these Mach numbers local regions of supersonic flow exist on the suction surface of the blade, and shock phenomena result at the points indicated previously by the pressure distribution in figure 11 (b).

Loss coefficient  $\frac{\bar{\omega}}{(p_t - p)_a}$ —The loss coefficient  $\frac{\omega}{(p_t - p)_a}$  has been computed from the total-pressure survey data taken downstream of the cascade for five values of  $M_d$  between 0.3 and 0.7. This loss coefficient is plotted in figure 13. The average total-pressure loss  $\bar{\omega}$  was calculated by methods given

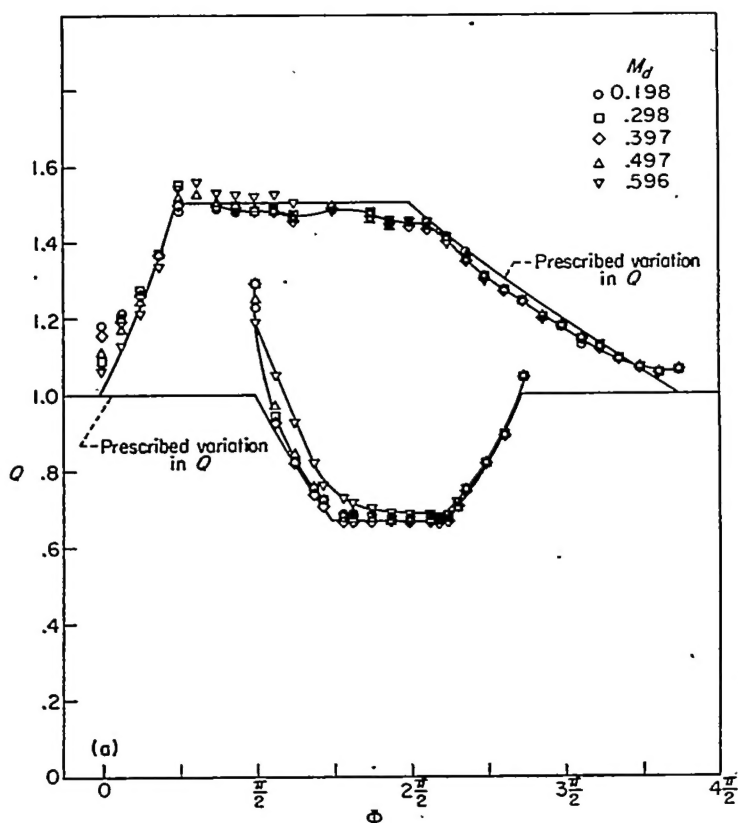
in appendix B. The loss coefficient at first decreases with increasing  $M_d$ , probably as a result of the increasing Reynolds number, and then increases rapidly, as a result of shock losses, after  $M_d$  equal to 0.6.

Turning angle  $\Delta\theta$ .—The measured value of the cascade turning angle  $\Delta\theta$  is plotted as a function of  $M_d$  in figure 14. The sudden increase in  $\Delta\theta$  as  $M_d$  approaches 0.6 is not reasonable in view of the small increase in loss coefficient (fig. 13) at this Mach number. The measured turning angle may therefore be inaccurate because of the adverse test conditions under which the data were recorded at high Mach numbers. In any event, for values of  $M_d$  less than 0.5 the turning angle is insensitive to Mach number, and the measured turning angle agreed within  $0.5^\circ$  with the design turning angle.

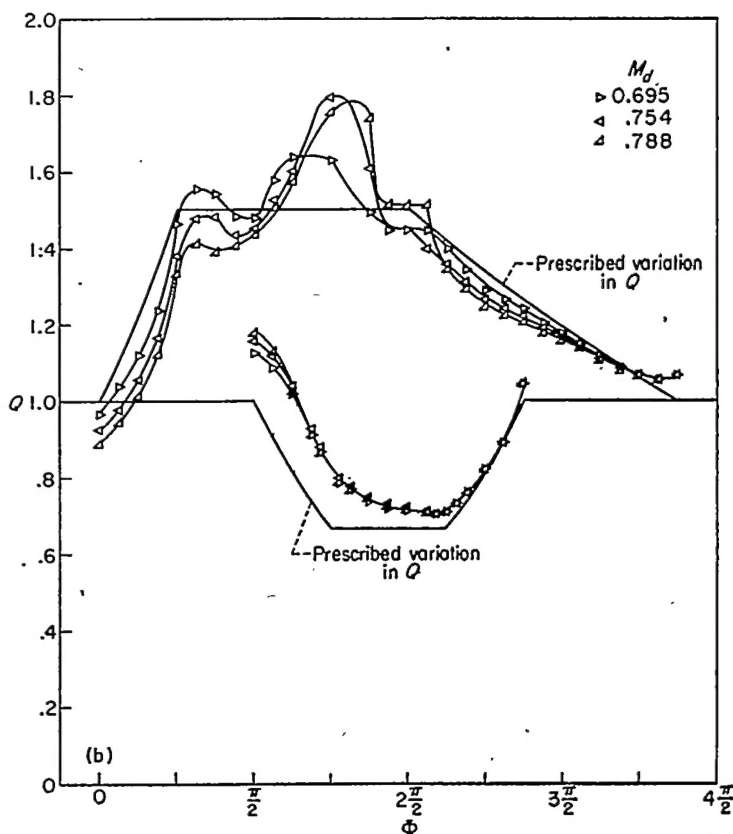
#### ANALYSIS OF RESULTS

The test results are analyzed for the continuity condition, compressibility effects, and momentum considerations. The cascade performance is then compared with that of similar cascades reported in the literature.

Continuity.—In figure 15 it is shown that, as the downstream Mach number  $M_d$  increases, the experimentally determined upstream Mach number  $M_u$  becomes progressively less than  $M_d$ . For an impulse cascade  $M_u$  should equal  $M_d$ , and the measured difference between  $M_d$  and  $M_u$  was sufficiently great to require an investigation of the continuity condition upstream and downstream of the cascade.



(a) Downstream Mach numbers between 0.2 and 0.6.



(b) Downstream Mach numbers of 0.70, 0.75, and 0.79.

FIGURE 12—Variation in test values of velocity  $Q$  with coordinate  $\Phi$  along surface of blade element. (The tap position corresponding to a given data point can be determined from the value of  $\Phi$  and table II.)

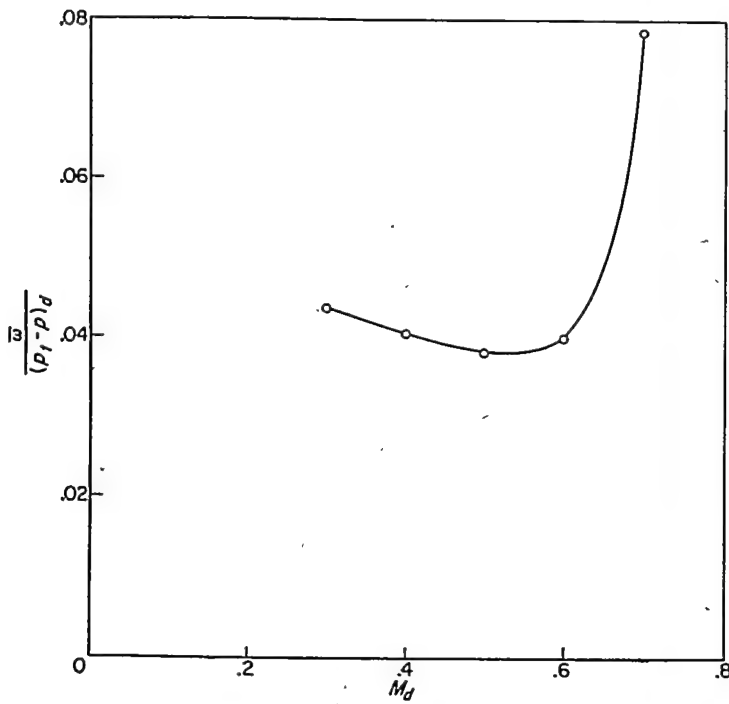


FIGURE 13.—Variation in pressure-loss coefficient with downstream Mach number.

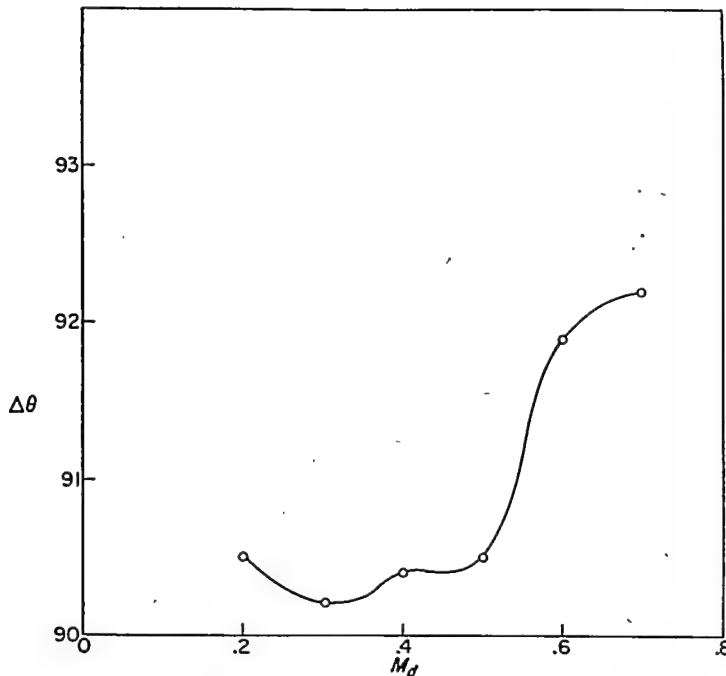


FIGURE 14.—Variation in air-turning angle with downstream Mach number.

From the total-pressure surveys downstream of the cascade, the velocity distribution is obtained as a function of  $y'/s'$ , where  $y'$  is measured from the center of a wake, and a typical example is given in figure 16 for a downstream Mach number of 0.3. (From the relatively small momentum losses indicated by this velocity distribution, it is concluded that boundary-layer separation on the blade surfaces was negligible.) From this velocity distribution the flow rate  $W$  through the channel between blades can be determined from the continuity equation

$$W_a = s' \int_0^{1.0} \rho'' q'' \cos \theta'_a d\left(\frac{y'}{s'}\right)$$

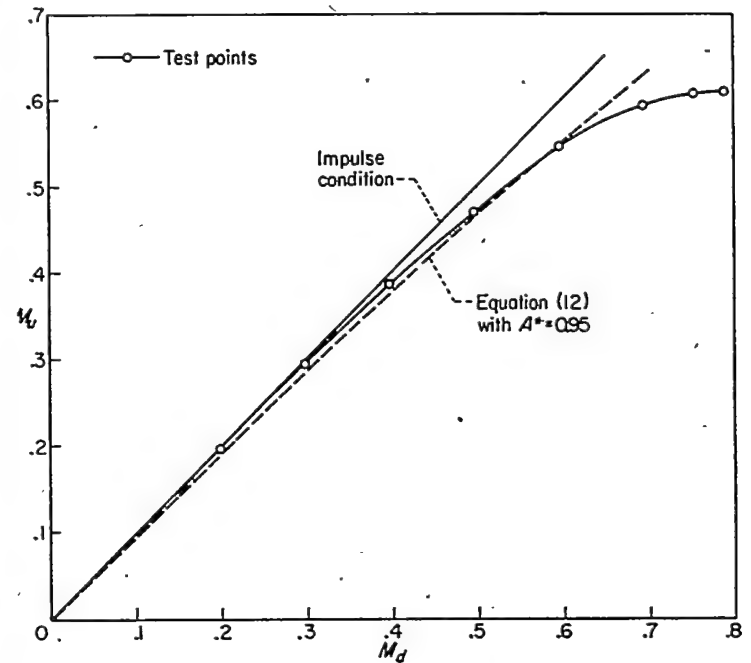
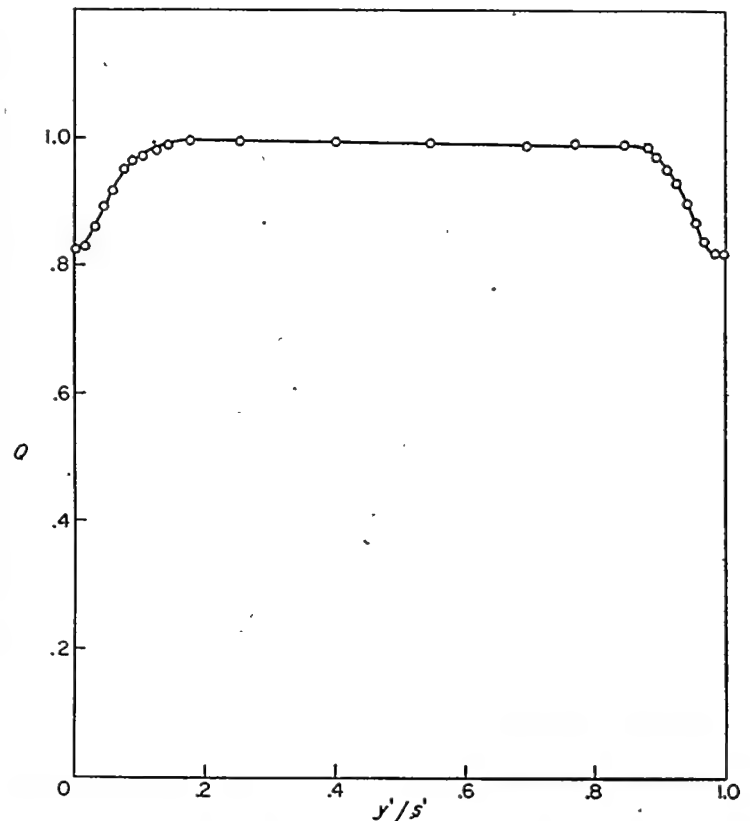


FIGURE 15.—Variation in upstream Mach number with downstream Mach number.

FIGURE 16.—Variation in  $Q$  with  $y'/s'$  between wakes downstream of cascade. Downstream Mach number  $M_d$ , 0.30.

where  $\rho''$  and  $q''$  are the density and velocity, respectively, in dimensional form and  $\theta'_a$  is the measured flow direction downstream of the cascade in the  $x'y'$ -plane. Upstream of the cascade, flow conditions are uniform and the continuity equation becomes

$$W_u = s'(\rho'' q'' \cos \theta')_u$$

The flow rates  $W_u$  and  $W_d$  are plotted in figure 17, and it is seen that the continuity condition ( $W_u = W_d$ ) is satisfied. The increasing magnitude of  $(M_d - M_u)$  with increasing  $M_d$  (fig. 15) must therefore be caused by the displacement of the wake downstream of the cascade.

If  $A^*$  is the ratio of the effective flow area (geometric area minus the effective displacement area of the wake) downstream of the cascade to the geometric area upstream of the cascade,  $M_d$  and  $M_u$  are related by (appendix C)

$$\frac{M_u}{M_d} = A^* \left( \frac{1 + \frac{\gamma-1}{2} M_u^2}{1 + \frac{\gamma-1}{2} M_d^2} \right)^{\frac{\gamma+1}{2(\gamma-1)}} \quad (12)$$

For an impulse cascade with no boundary layer,  $A^*$  equals 1.0 and from equation (12)  $M_u$  is equal to  $M_d$ . If, however, the effective displacement of the boundary layer is 5 percent,  $A^*$  is equal to 0.95 and the relation between  $M_u$  and  $M_d$  is given by the dashed curve in figure 15. Thus, for a given value of  $A^*$  a cascade designed for impulse operation without a wake exhibits progressively more reaction as the downstream Mach number increases.

In figure 15 for values of  $M_d$  greater than 0.75, the value of  $M_u$  remains essentially constant and equal to 0.6, or a little higher, so that the cascade is choked. In figure 12 the high value for  $Q$  on the pressure surface at  $\Phi$  equal to  $\pi/2$  indicates that the choke condition occurs along this value of  $\Phi$ . Figure 6 shows that for this value of  $\Phi$  the flow area of the channel between blade elements is a minimum. Thus the upstream Mach number for choke flow could probably be increased by a slight modification in the blade-element design in the regions of  $\Phi$  equal to  $\pi/2$ . (For example, the manner in which the blade nose is rounded off might be modified to increase the minimum flow area. Also, the blade nose might be extended farther upstream along the channel boundaries (shown in fig. 6) to guide the fluid into the minimum area in the proper direction. Or perhaps near the nose a less rapid velocity deceleration might be prescribed on the pressure surface, or a less rapid acceleration on the suction surface, so that the rate of area convergence and divergence in the vicinity of the minimum area would be reduced.) In addition this design modification would eliminate the large deceleration of the velocity along the pressure surface following the peak velocity at  $\Phi$  equal to  $\pi/2$  and might thus improve the efficiency of the cascade by eliminating a possible region of separated boundary layer.

**Compressibility effects.**—The effects of compressibility on  $P$  and  $Q$  are shown by the effects of  $M_d$  in figures 11 and 12. Consider the region of constant prescribed velocity along the suction surface. Provided the local velocities are subsonic, the absolute magnitude of the pressure coefficient  $P$  decreases with increasing  $M_d$  (fig. 11(a)), but the velocity  $Q$  remains essentially unchanged (fig. 12(a)). This behavior of  $P$  and  $Q$  is unlike that for isolated blades (airfoils), but compares favorably with that for the known compressible flow between a curved channel consisting of streamlines from a free compressible vortex. (The regions of constant velocity along the pressure and suction surfaces of the blades

suggest that the channel between these regions can be approximated by the flow between selected streamlines of a free vortex.) In appendix D equations are derived for computing the variation in  $P$  and  $Q$  with the equivalent  $M_d$  for those radii of a free compressible vortex for which the values of  $P$  and  $Q$  at  $M_d$  equal to zero (incompressible flow) are the prescribed values for the cascade design ( $Q_{max}=1.5$ ,  $Q_{min}=0.66687$ , and so forth). The resulting distributions in  $Q$  and  $P$  with  $M_d$  for the compressible vortex are shown in figures 18 and 19, respectively, and are compared with the test values of  $Q$  and  $P$  at taps 44 and 20 (see table II) on the pressure and suction surfaces of the blades, respectively. The agreement in trends is good and indicates that the observed variations in  $P$  and  $Q$  with  $M_d$  in the tests are reasonable. Thus, for the high-solidity impulse cascade of this report the distribution of  $Q$  is essentially independent of downstream Mach number  $M_d$ .

The appearance of supersonic velocities on the suction surface of the blade is indicated (in figs. 11(b) and 12(b)) by sizeable variations in  $P$  and  $Q$  (with  $x'/c$  and  $\Phi$ , respectively) due to shock phenomena. For a given value of  $M_d$  there is a critical value of  $Q$  ( $Q_{cr}$ ) for which the velocity corresponding to  $Q_{cr}$  is sonic. This relation is given by (appendix E)

$$Q_{cr} = \sqrt{\frac{1 + \frac{\gamma-1}{2} M_d^2}{\frac{\gamma+1}{2} M_d^2}} \quad (13)$$

which is plotted in figure 20. For test values of  $Q$  about equal to 1.5, such as exist on the suction surface at  $\Phi$  equal to  $\pi/4$ , the value of  $M_d$  in figure 20 is about 0.63. Thus in figures 11 (b) and 12 (b) shock phenomena are observed for values of  $M_d$  equal to 0.70, 0.75, and 0.79.

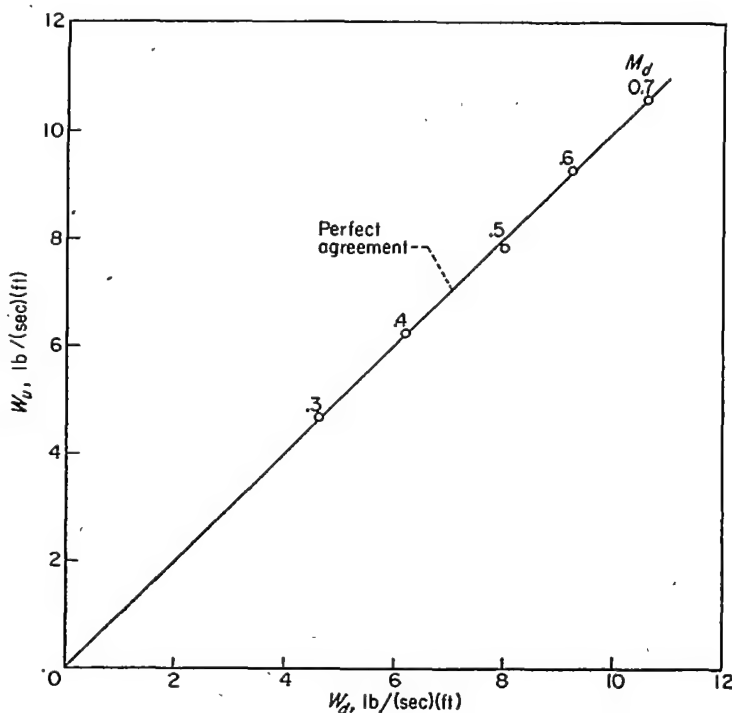


FIGURE 17.—Comparison of measured flow rates upstream and downstream of cascade for five values of downstream Mach number.



**Momentum.**—From momentum considerations it can be shown (appendix F) that the blade force in the direction of  $y'$  (per unit length of blade span) is equal to

$$F_y = \frac{s' \sin \theta'_a \cos \theta'_a}{g} \int_0^{1.0} \rho''_a (q''_a)^2 d\left(\frac{y'}{s'}\right) - \frac{s' \sin \theta'_u \cos \theta'_u}{g} \rho''_u (q''_u)^2 \quad (14)$$

where  $\rho''$  and  $q''$  are evaluated from the test data by equations (B2), (B3), and (B5) of appendix B, and the known value of the stagnation speed of sound  $a_0$ .

From the measured pressures on the blade surface, the blade force  $F_y$  is also equal to

$$F_y = c(p_{t,a} - p_a) \int_{nose}^{tail} \left( \frac{P_{\pi/2} - P_0}{2} \right) d\left(\frac{x'}{c}\right) \quad (15)$$

where the subscripts  $\pi/2$  and 0 refer to the pressure and suction surfaces of the blade, respectively, and where for a given  $M_d$  the integral is equal to the area under the curve in figure 11. The blade force  $F_y$  has been computed from the test data by equations (14) and (15), and the values are compared in figure 21. The agreement is considered satisfactory and serves as a check on the accuracy of the experimental data.

**Comparison with other impulse cascades.**—The test performance [ $\Delta\theta$  and minimum  $\bar{\omega}/(p_t - p_a)$ ] of the  $90^\circ$  impulse cascade given in this report is compared in the following table with that of other impulse cascades reported in the literature:

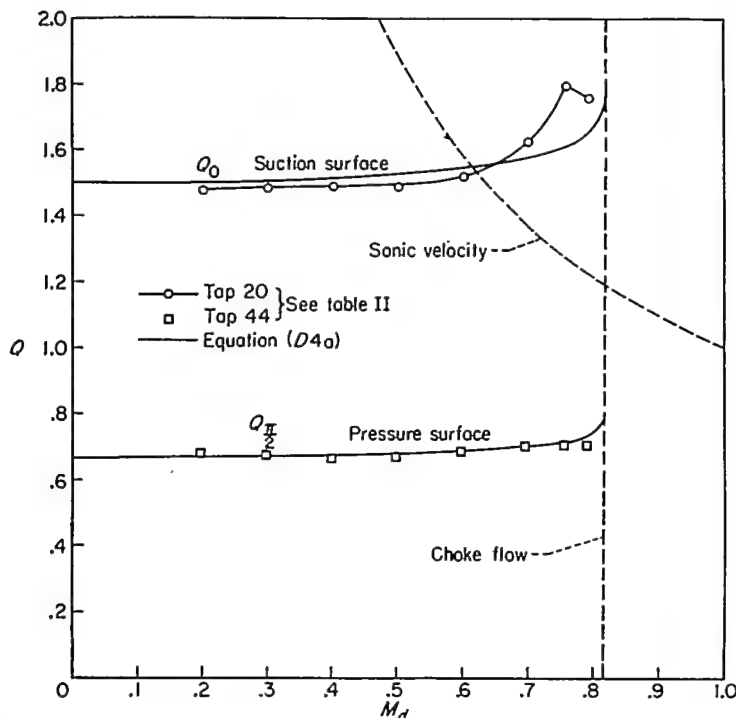


FIGURE 18.—Variation in velocity  $Q$  with downstream Mach number  $M_d$  at static taps on pressure and suction surfaces of blade and at equivalent radii of a free compressible vortex.

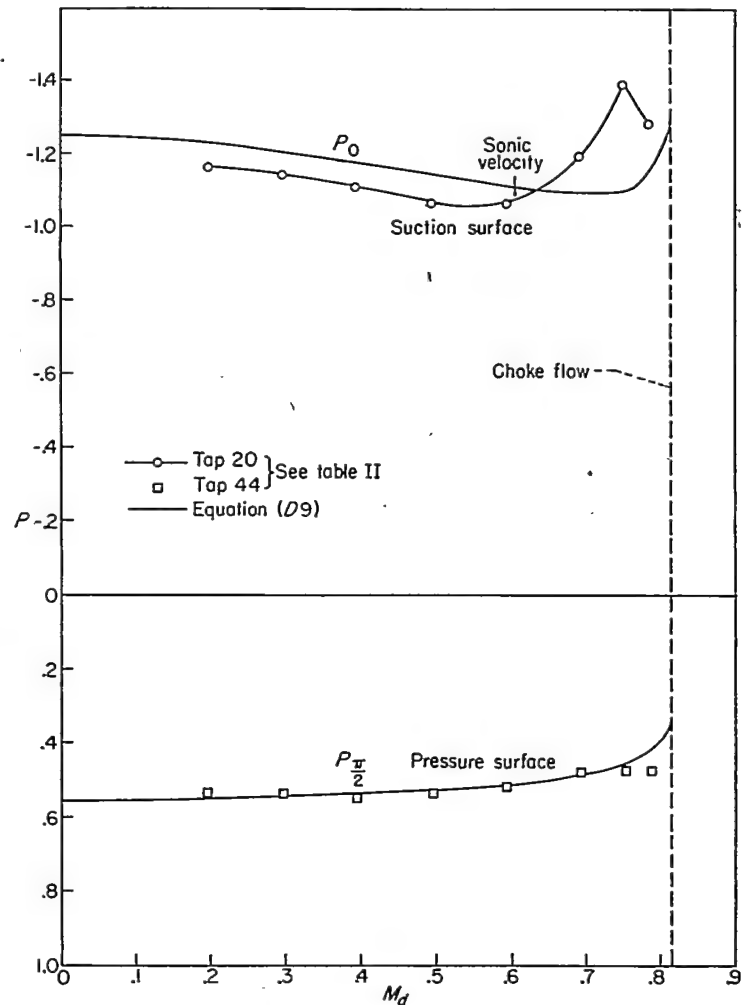


FIGURE 19.—Variation in pressure coefficient  $P$  with downstream Mach number  $M_d$  at static taps on pressure and suction surface of blade and at equivalent radii of a free compressible vortex.

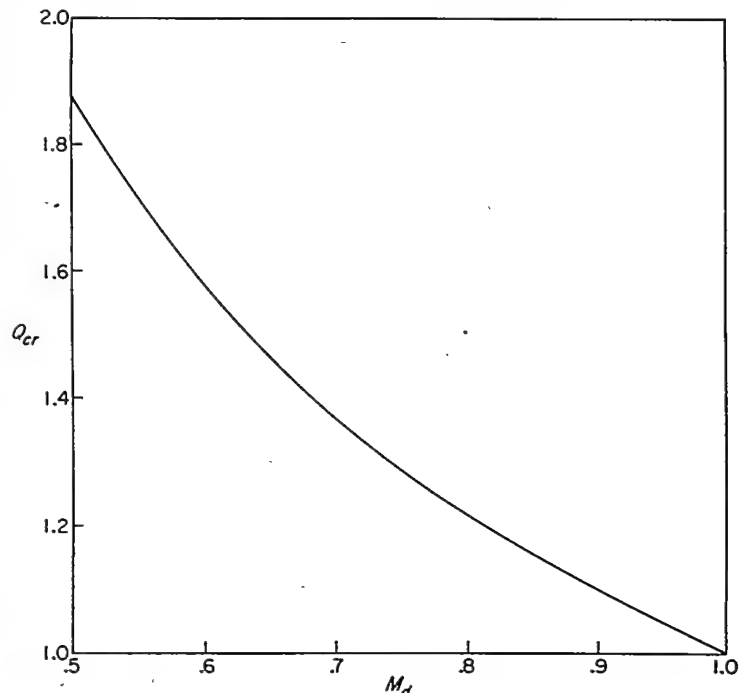


FIGURE 20.—Variation in  $Q_{cr}$  with downstream Mach number. (For a given value of  $M_d$  sonic velocity occurs for  $Q$  equal to  $Q_{cr}$ .)

Blade	Inverse of solidity, $s/c$	Loss coefficient, $\frac{\bar{w}}{(p_t - p)_a}$	Turning angle, $\Delta\theta$ , deg	Reynolds number, $Re$	Comments	Reference
A-----	0.750	0.035 (min.)-----	90	$2 \times 10^5$ -----	Airfoil blading $t/c=0.10$ -----	13, fig. 62
B-----	.750	0.035-----	86	Low speed-----	Blade shape similar to blade C-----	15, fig. 178
C-----	.613	0.038 (min.)-----	90.5	$1.5 \times 10^5$ -----	Designed for prescribed velocity gradients that avoid separation-----	This report
D-----	.500	0.038-----	87	Low speed-----	Airfoil blading-----	15, fig. 177
E-----	.500	0.039 (min.)-----	90	$2 \times 10^5$ -----	Airfoil blading, $t/c=0.10$ -----	13, fig. 62
F-----	.574	0.05-----	88.6	$1.8 \times 10^5$ -----	Two circular arcs plus flat section, similar to blade C-----	6, p. 4
G-----	.625	0.072 (min.)-----	90	$2 \times 10^5$ -----	"Conventional" impulse blade, $t/c=0.22$ -----	13, fig. 62
H-----	.500	0.09-----	88.7	$1.8 \times 10^5$ -----	Two circular arcs, sharp nose and tail, symmetrical-----	6, p. 4

The blades A to H are arranged in order of increasing minimum loss coefficient  $\frac{\bar{w}}{(p_t - p)_a}$ . All cascades have approximately a  $90^\circ$  turning angle. Blade C, from this report, is seen to have about as low losses as any reported in the literature. The low loss coefficients of blades A and E are questioned in reference 13 (p. 233) because of the experimental technique. Also, the thin profiles (small values of  $t/c$ , where  $t$  is the maximum blade thickness) of blades A, D, and E prohibit their use in turbines near the blade root (where impulse conditions are usually approached) because the blade taper requires thicker profiles at the root. Blade B has a thicker profile and gives excellent performance. It is similar in shape and performance to blade C, developed in this report.

It is concluded that, if properly applied, the high-solidity blade-element design method developed in this report can result in efficient blade profiles for incompressible flow or for compressible flow with local subsonic velocities. These profiles can be designed directly without extensive experimental trial-and-error development.

#### SUMMARY OF RESULTS AND CONCLUSIONS

A technique is developed for application of a channel design method to the design of high-solidity cascades with prescribed velocity distributions as a function of arc length along the blade-element profile and for prescribed turning angles of the fluid. The technique applies to both incompressible and subsonic compressible (ratio of specific heats equal to  $\gamma=1.0$ ) fluid motion, and the results are exact except for the usual approximation resulting from rounding off the nose and tail of the blade element. In order to investigate the effect on the velocity distribution of rounding off the nose and tail, a high-solidity  $90^\circ$  impulse cascade was designed and tested. To achieve good efficiency, the cascade was designed for prescribed velocities with maximum allowable blade loading according to limitations imposed by considerations of boundary-layer separation. The cascade was developed for incompressible flow and was tested at the design angle of attack over a range of downstream Mach

numbers from 0.2 to choke flow. From the results of the tests it is concluded that:

1. Blades for high-solidity cascades can be designed for prescribed velocities by the channel flow methods of this report.
2. Rounding off the nose and tail of the blade-element profile has negligible effect on the velocity distribution along the blade surface except in the vicinity of the blade nose.
3. The distribution of the velocity (expressed as a ratio of the downstream velocity) is essentially independent of downstream Mach number, provided the maximum velocity on the blade surface is subsonic.
4. For the velocity distribution that was prescribed (and measured), the boundary-layer separation on the blade surfaces was negligible.
5. For downstream Mach numbers of 0.5 or less the measured turning angle was less than  $0.5^\circ$  greater than the design turning angle ( $90^\circ$ ).

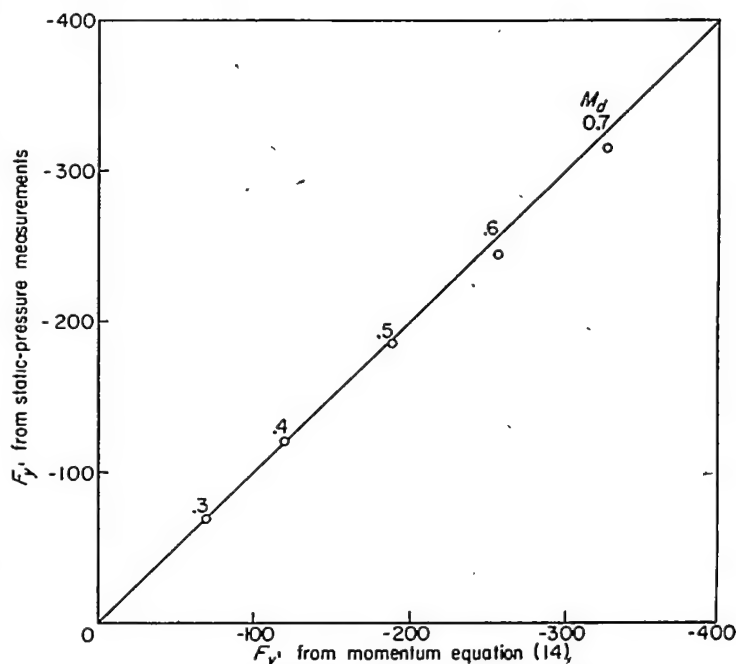


FIGURE 21.—Comparison of blade force in direction of  $y'$  as determined from measured static pressures on blade surface and from momentum equation (14).

6. The cascade choked near the inlet at an upstream Mach number slightly greater than 0.6. This Mach number for choke could probably be increased by a modification in the profile design near the blade nose.

7. Sonic velocity first appears on the suction surface of the blade at a downstream Mach number of about 0.63 and for downstream Mach numbers of 0.70, 0.75, and 0.79 shock phenomena were observed on the blade surfaces.

8. A cascade designed for impulse operation without a boundary layer exhibits progressively more reaction in the presence of a constant wake displacement as the downstream Mach number increases.

9. If properly applied, the high-solidity blade-element design method developed in this report can result in efficient blade profiles for incompressible flow or for compressible flow with local subsonic velocities. These profiles can be designed directly without extensive experimental trial-and-error development.

LEWIS FLIGHT PROPULSION LABORATORY,  
NATIONAL ADVISORY COMMITTEE FOR AERONAUTICS,  
CLEVELAND, OHIO, November 30, 1951.

## APPENDIX A

### SYMBOLS

The following symbols are used in this report:

$A^*$	ratio of flow area downstream of cascade to flow area upstream
$a$	local speed of sound
$a_o$	stagnation speed of sound
$c$	blade chord (fig. 7)
$F_v$	blade force in direction of $y'$
$g$	gravitational acceleration
$K_1, K_2$	constants, eqs. (D1a) and (D4a), respectively, of appendix D
$M$	Mach number, $q''/a$
$P$	pressure coefficient, eq. (11)
$p$	static pressure (dimensional form)
$\Delta p_i$	loss in total pressure at point downstream of cascade
$Q$	velocity (for which units are so chosen that channel velocity downstream at infinity is unity)
$Q_{cr}$	critical value of $Q$ for which velocity corresponding to $Q_{cr}$ is sonic; related to $M_a$ by eq. (13)
$q$	velocity (for which units are so chosen that stagnation speed of sound is unity)
$q''$	velocity (dimensional form)
$R$	perfect gas constant
$Re$	Reynolds number based on blade chord
$r$	radius from center of free vortex (for which radius the units are so chosen that width, downstream at infinity, of channel between cascade blades that is being simulated by free vortex is unity)
$s$	distance in $xy$ -plane measured along direction of flow from arbitrary reference point (for which distance the units are so chosen that channel width downstream at infinity is unity)
$s'$	blade spacing (fig. 7)
$T$	temperature of gas
$t$	maximum thickness of blade-element profile
$V$	velocity parameter defined in ref. 11
$W$	flow rate (per unit length of blade span) through channel between two blade elements

$x, y$	Cartesian coordinates in physical plane (for which coordinates the units are so chosen that channel width downstream at infinity is unity)
$x', y'$	$x, y$ -coordinate system rotated and translated so that cascade lies along $y'$ -axis (fig. 7)
$\beta'_{nose}, \beta'_{tail}$	average angle of blade surfaces tangent to circular arcs at nose and tail, respectively, in $x'y'$ -plane (fig. 7)
$\gamma$	ratio of specific heats
$\Delta$	finite increment
$\theta$	flow direction in physical $xy$ -plane (measured in counterclockwise direction from positive $x$ -axis)
$\Delta\theta$	channel, or cascade, turning angle
$\theta'$	flow direction in physical $x'y'$ -plane (measured counterclockwise from positive $x'$ -axis)
$\lambda$	ratio of arc lengths, eq. (7)
$\rho$	density (expressed as ratio of stagnation density)
$\rho''$	density (dimensional form)
$\Phi, \Psi$	velocity potential and stream function, respectively, used as Cartesian coordinates in transformed $\Phi\Psi$ -plane and defined in ref. 11
$\bar{\omega}$	average loss in total pressure, eq. (B1) of appendix B
Subscripts:	
$A, B, \dots, H$	positions defined by velocity potential lines in fig. 2
$CC, DD, EE, FF$	values of $\Phi$ defined in fig. 4
$d$	conditions downstream at infinity
$max$	maximum
$min$	minimum
$t$	total, or stagnation, condition
$u$	conditions upstream at infinity
$0$	right boundary of channel, when faced in direction of flow, along which $\Psi$ is equal to zero
$\frac{\pi}{2}$	left boundary of channel, when faced in direction of flow, along which $\Psi$ is equal to $\pi/2$

## APPENDIX B

CALCULATION OF AVERAGE LOSS IN TOTAL PRESSURE  $\bar{\omega}$  FROM TOTAL-PRESSURE SURVEY DOWNSTREAM OF CASCADE

By definition the mass-weighted average value of the loss in total pressure  $(\Delta p_{t,d})$  downstream of the cascade is

$$\bar{\omega} = \frac{\int \rho'' q (\Delta p_{t,d}) dy'}{\int \rho'' q dy'} \quad (B1)$$

where the integration is taken across an entire channel equal in width to the blade spacing and therefore including the wake region. The density  $\rho''$  is related to the pressure  $p$  by

$$\frac{\rho''}{\rho''_t} = \left( \frac{p}{p_t} \right)^{\frac{1}{\gamma}} \quad (B2)$$

where, from the perfect gas law,

$$\rho''_t = \frac{p_t}{RT_t} \quad (B3)$$

Also, from the general energy equation,

$$\frac{T}{T_t} = 1 - \frac{\gamma-1}{2} q^2 \quad (B4)$$

where  $T$  is the temperature of the gas and  $\gamma$  is the ratio of specific heats, so that

$$\frac{p}{p_t} = \left( \frac{T}{T_t} \right)^{\frac{\gamma}{\gamma-1}} = \left( 1 - \frac{\gamma-1}{2} q^2 \right)^{\frac{\gamma}{\gamma-1}}$$

from which

$$q = \sqrt{\frac{2}{\gamma-1} \left[ 1 - \left( \frac{p}{p_t} \right)^{\frac{\gamma-1}{\gamma}} \right]} \quad (B5)$$

Thus, from equations (B1), (B2), (B3), and (B5)

$$\bar{\omega} = \frac{\int p_t (\Delta p_t) \left( \frac{p_d}{p_t} \right)^{\frac{1}{\gamma}} \sqrt{1 - \left( \frac{p_d}{p_t} \right)^{\frac{\gamma-1}{\gamma}}} dy'}{\int p_t \left( \frac{p_d}{p_t} \right)^{\frac{1}{\gamma}} \sqrt{1 - \left( \frac{p_d}{p_t} \right)^{\frac{\gamma-1}{\gamma}}} dy'} \quad (B6)$$

where  $p_t$  is the total pressure measured by the survey along  $y'$ .

## APPENDIX C

RELATION BETWEEN  $M_u$  AND  $M_d$  FOR VARIOUS AREA RATIOS  $A^*$ 

From continuity considerations

$$\rho_u (Ma)_u = \rho_d (Ma)_d A^* \quad (C1)$$

where  $\rho$  is the fluid density expressed as a ratio of the stagnation density,  $M$  is the local Mach number,  $a$  is the local speed of sound so that the product  $(Ma)$  is equal to the velocity  $q''$ , and  $A^*$  is the ratio of the effective downstream flow area to the upstream area. From the general energy equation,

$$\frac{T_t}{T} = 1 + \frac{\gamma-1}{2} M^2 \quad (C2)$$

so that

$$\frac{a_d}{a_u} = \sqrt{\frac{T_d}{T_u}} = \sqrt{\frac{1 + \frac{\gamma-1}{2} M_u^2}{1 + \frac{\gamma-1}{2} M_d^2}}$$

and

$$\frac{\rho_d}{\rho_u} = \left( \frac{T_d}{T_u} \right)^{\frac{1}{\gamma-1}} = \left( \frac{1 + \frac{\gamma-1}{2} M_u^2}{1 + \frac{\gamma-1}{2} M_d^2} \right)^{\frac{1}{\gamma-1}}$$

from which equation (C1) becomes

$$M_u = M_d A^* \left( \frac{1 + \frac{\gamma-1}{2} M_u^2}{1 + \frac{\gamma-1}{2} M_d^2} \right)^{\frac{\gamma+1}{2(\gamma-1)}} \quad (12)$$

## APPENDIX D

## EQUIVALENT COMPRESSIBLE FREE VORTEX

The regions of constant, prescribed velocity along the pressure and suction surfaces of the 90° impulse blade suggest that, for purposes of investigating the variation in these velocities with the equivalent downstream Mach number, the channel between these regions of constant velocity can be approximated by the flow between selected streamlines of a compressible free vortex. First, the radii for these selected streamlines are determined for an incompressible free vortex to give the prescribed values of  $Q_0$  and  $Q_{\frac{\pi}{2}}$  for incompressible

flow along the suction and pressure surfaces of the blade, respectively.

**Incompressible free vortex.**—For an incompressible free vortex

$$Qr = K_1 \quad (D1a)$$

so that

$$Q_0 r_0 = Q_{\frac{\pi}{2}} r_{\frac{\pi}{2}} \quad (D1b)$$

where  $r$ , like the Cartesian coordinates  $x$  and  $y$ , is expressed



in units of the channel width downstream at infinity of the channel between cascade blades that is being simulated by the free vortex. From continuity

$$\int_{r_0}^{r_{\frac{\pi}{2}}} Q dr = 1.0 \quad (D2)$$

so that, from equations (D1a) and (D2),

$$K_1 \log_e \frac{r_{\frac{\pi}{2}}}{r_0} = 1.0$$

and therefore, from equations (D1a) and (D1b),

$$r_0 = \frac{1}{Q_0 \log_e \frac{Q_0}{Q_{\frac{\pi}{2}}}} \quad (D3a)$$

and

$$r_{\frac{\pi}{2}} = \frac{1}{Q_{\frac{\pi}{2}} \log_e \frac{Q_0}{Q_{\frac{\pi}{2}}}} \quad (D3b)$$

Equations (D3a) and (D3b) give the radii that determine the channel in the free vortex (compressible or incompressible) which is equivalent to the channel between the cascade blades in the region of constant prescribed velocity along the pressure and suction surfaces. For the prescribed values of  $Q_0$  and  $Q_{\frac{\pi}{2}}$  (1.5 and 0.66687, respectively) the values of  $r_0$  and  $r_{\frac{\pi}{2}}$  given by equations (D3a) and (D3b) are 0.82260 and 1.84992, respectively.

**Compressible free vortex.**—For a compressible free vortex

$$Qr = K_2 \quad (D4a)$$

so that

$$Q_0 r_0 = Q_{\frac{\pi}{2}} r_{\frac{\pi}{2}} \quad (D4b)$$

and, from continuity,

$$\int_{r_0}^{r_{\frac{\pi}{2}}} \rho Q dr = \rho_a \quad (D5)$$

where, from equation (B4),

$$\rho = \left( \frac{T}{T_i} \right)^{\frac{1}{\gamma-1}} = \left( 1 - \frac{\gamma-1}{2} Q^2 q_a^2 \right)^{\frac{1}{\gamma-1}} \quad (D6a)$$

so that

$$\rho_a = \left( 1 - \frac{\gamma-1}{2} q_a^2 \right)^{\frac{1}{\gamma-1}} \quad (D6b)$$

Equation (D6a) expands in series form to give

$$\rho = 1 - \frac{1}{2} Q^2 q_a^2 + \frac{2-\gamma}{8} Q^4 q_a^4 - \dots \quad (D6c)$$

so that equation (D5), together with equations (D4a), (D6b), and (D6c), integrates to give

$$\begin{aligned} \rho_a = \left( 1 - \frac{\gamma-1}{2} q_a^2 \right)^{\frac{1}{\gamma-1}} &= K_2 \log_e \frac{r_{\frac{\pi}{2}}}{r_0} + \frac{q_a^2 K_2^3}{4} \left( \frac{1}{r_{\frac{\pi}{2}}^2} - \frac{1}{r_0^2} \right) - \\ &\frac{(2-\gamma)}{32} q_a^4 K_2^5 \left( \frac{1}{r_{\frac{\pi}{2}}^4} - \frac{1}{r_0^4} \right) + \dots \end{aligned} \quad (D7)$$

where, from equation (C2),

$$q_a = M_a \sqrt{\frac{T_a}{T_i}} = \frac{M_a}{\sqrt{1 + \frac{\gamma-1}{2} M_a^2}} \quad (D8)$$

From equations (D7) and (D8)  $K_2$  is a known function of  $M_a$  and therefore  $Q_0$  and  $Q_{\frac{\pi}{2}}$  are given by equation (D4a). The variation in  $Q_0$  and  $Q_{\frac{\pi}{2}}$  with  $M_a$  is plotted in figure 18.

The pressure coefficient  $P$  is defined by

$$P = \frac{p - p_a}{p_{t,a} - p_a} = \frac{\frac{p}{p_{t,a}} - \frac{p_a}{p_{t,a}}}{1 - \frac{p_a}{p_{t,a}}}$$

where, from equation (B4),

$$\frac{p}{p_{t,a}} = \left( \frac{T}{T_i} \right)^{\frac{\gamma}{\gamma-1}} = \left( 1 - \frac{\gamma-1}{2} Q^2 q_a^2 \right)^{\frac{\gamma}{\gamma-1}}$$

so that, with  $p_i = p_{t,a}$ ,

$$P = \frac{\left( 1 - \frac{\gamma-1}{2} Q^2 q_a^2 \right)^{\frac{\gamma}{\gamma-1}} - \left( 1 - \frac{\gamma-1}{2} q_a^2 \right)^{\frac{\gamma}{\gamma-1}}}{1 - \left( 1 - \frac{\gamma-1}{2} q_a^2 \right)^{\frac{\gamma}{\gamma-1}}} \quad (D9)$$

Equation (D9) determines  $P$  for given values of  $Q$  and  $q_a$ . The variation in  $P_0$  and  $P_{\frac{\pi}{2}}$  with  $M_a$  is plotted in figure 19.

**Choke flow.**—Choke, or maximum, flow occurs when the derivative of the flow rate with respect to a characteristic velocity is zero. From equation (D5) the flow rate is proportional to  $\rho_a$ , and from equation (D4a) the velocity at each radius is proportional to  $K_2$  so that choke flow occurs when

$$\frac{d\rho_a}{dK_2} = 0$$

Therefore, from equation (D7)

$$0 = \log_e \frac{r_{\frac{\pi}{2}}}{r_0} + \frac{3q_a^2 K_2^3}{4} \left( \frac{1}{r_{\frac{\pi}{2}}^2} - \frac{1}{r_0^2} \right) - \frac{5(2-\gamma)}{32} q_a^4 K_2^5 \left( \frac{1}{r_{\frac{\pi}{2}}^4} - \frac{1}{r_0^4} \right) + \dots$$

or

$$\begin{aligned} q_a^2 K_2^2 = & \frac{\frac{3}{4} \left( \frac{1}{r_{\frac{\pi}{2}}^2} - \frac{1}{r_0^2} \right) - \sqrt{\frac{9}{16} \left( \frac{1}{r_{\frac{\pi}{2}}^2} - \frac{1}{r_0^2} \right)^2 + \frac{5(2-\gamma)}{8} \left( \frac{1}{r_{\frac{\pi}{2}}^4} - \frac{1}{r_0^4} \right) \log_e \frac{r_{\frac{\pi}{2}}}{r_0}}}{\frac{5(2-\gamma)}{16} \left( \frac{1}{r_{\frac{\pi}{2}}^4} - \frac{1}{r_0^4} \right)} \end{aligned} \quad (D10)$$

The value of  $M_a$  for choke flow is then obtained from equations (D7), (D8), and (D10). For the values of  $r_0$  and  $r_{\frac{\pi}{2}}$  given by equations (D3a) and (D3b), the value of  $M_a$  thus obtained is 0.815.

## APPENDIX E

CRITICAL VALUE OF  $Q$  FOR WHICH VELOCITY IS SONIC

For a given value of  $M_d$  there is a critical value of  $Q$  ( $Q_{cr}$ ) for which the velocity corresponding to  $Q_{cr}$  is sonic. By definition

$$Q = \frac{q}{q_d} = \frac{M}{M_d} \sqrt{\frac{T}{T_d}}$$

which, from equation (C2), becomes

$$Q = \frac{M}{M_d} \sqrt{\frac{1 + \frac{\gamma-1}{2} M_d^2}{1 + \frac{\gamma-1}{2} M^2}} \quad (E1)$$

By definition  $Q$  is equal to  $Q_{cr}$  if  $M$  is equal to 1.0 so that equation (E1) becomes

$$Q_{cr} = \sqrt{\frac{1 + \frac{\gamma-1}{2} M_d^2}{\frac{\gamma+1}{2} M_d^2}} \quad (13)$$

Equation (13) gives the relation between  $Q_{cr}$  and  $M_d$ , which relation is plotted in figure 20.

## APPENDIX F

## BLADE FORCE COMPUTED FROM MOMENTUM CONSIDERATIONS

If the viscous shear forces, which are relatively small, are ignored, the blade force  $F_y$ , acting on the fluid in the positive  $y'$ -direction (fig. 7) must, from momentum considerations, equal the change in the rate of momentum, in the positive  $y'$ -direction, of the fluid flowing through the cascade. The rate of momentum flow into the cascade in the positive  $y'$ -direction is

$$\frac{s' \sin \theta'_u \cos \theta'_u}{g} = \rho''_u (q''_u)^2$$

where flow conditions are considered uniform upstream of the cascade, and the rate of momentum flow out of the cascade in the positive  $y'$ -direction is

$$\frac{s' \sin \theta'_d \cos \theta'_d}{g} \int_0^{1.0} \rho''_d (q''_d)^2 d\left(\frac{y'}{s'}\right)$$

where the flow direction is uniform at a station far enough downstream. Therefore,  $F_y$  becomes

$$F_y = \frac{s' \sin \theta'_d \cos \theta'_d}{g} \int_0^{1.0} \rho''_d (q''_d)^2 d\left(\frac{y'}{s'}\right) - \frac{s' \sin \theta'_u \cos \theta'_u}{g} \rho''_u (q''_u)^2 \quad (14)$$

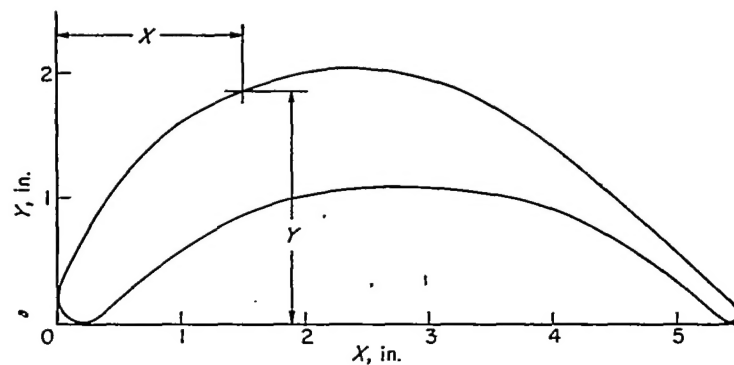
Equation (14) gives the component of the blade force in the positive direction of  $y'$ .

## REFERENCES

1. Lighthill, M. J.: A Mathematical Method of Cascade Design. R. & M. No. 2104, British A. R. C., June 1945.
2. Hansen, Arthur G., and Yohner, Peggy L.: A Numerical Procedure for Designing Cascade Blades with Prescribed Velocity Distributions in Incompressible Potential Flow. NACA TN 2101, 1950.
3. Goldstein, Arthur W., and Jerison, Meyer: Isolated and Cascade Airfoils with Prescribed Velocity Distribution. NACA Rep. 869, 1947. (Supersedes NACA TN 1308.)
4. Costello, George R.: Method of Designing Cascade Blades with Prescribed Velocity Distributions in Compressible Potential Flows. NACA Rep. 978, 1950. (Supersedes NACA TN's 1913 and 1970.)
5. Costello, George R., Cummings, Robert L., and Sinnette, John T., Jr.: Detailed Computational Procedure for Design of Cascade Blades with Prescribed Velocity Distributions in Compressible Potential Flows. NACA Rep. 1060, 1952. (Supersedes NACA TN 2281.)
6. Collar, A. R.: Some Experiments with Cascades of Aerofoils. R. & M. No. 1768, British A. R. C., Dec. 1936.
7. Wu, Chung-Hua, and Brown, Curtis A.: A Method of Designing Turbomachine Blades with a Desirable Thickness Distribution for Compressible Flow Along an Arbitrary Stream Filament of Revolution. NACA TN 2455, 1951.
8. Huppert, M. C., and MacGregor, Charles: Comparison Between Predicted and Observed Performance of Gas-Turbine Stator Blade Designed for Free-Vortex Flow. NACA TN 1810, 1949.
9. Alpert, Sumner: Design Method for Two-Dimensional Channels for Compressible Flow with Application to High-Solidity Cascades. NACA TN 1931, 1949.
10. Stanitz, John D.: Approximate Design Method for High-Solidity Blade Elements in Compressors and Turbines. NACA TN 2408, 1951.
11. Stanitz, John D.: Design of Two-Dimensional Channels with Prescribed Velocity Distributions Along the Walls. NACA Rep. 1115, 1953. (Supersedes NACA TN's 2593 and 2595.)
12. Goldstein, Arthur W., and Mager, Artur: Attainable Circulation about Airfoils in Cascade. NACA Rep. 953, 1950. (Supersedes NACA TN 1941.)
13. Ainley, D. G.: Performance of Axial-Flow Turbines. War Emergency Issue No. 41 pub. by Inst. Mech. Eng. (London). (Reprinted in U. S. by A. S. M. E., April 1949, pp. 230-244.)
14. Howell, A. R.: The Present Basis of Axial Flow Compressor Design. Part I. Cascade Theory and Performance. R. & M. No. 2095, British A. R. C., June 1942.
15. Reeman, J.: The Turbine for the Simple Jet Propulsion Engine. War Emergency Issue No. 12 pub. by Inst. Mech. Eng. (London), 1945. (Reprinted in U. S. by A. S. M. E., Jan. 1947, pp. 495-504.)

TABLE I.—BLADE PROFILE COORDINATES

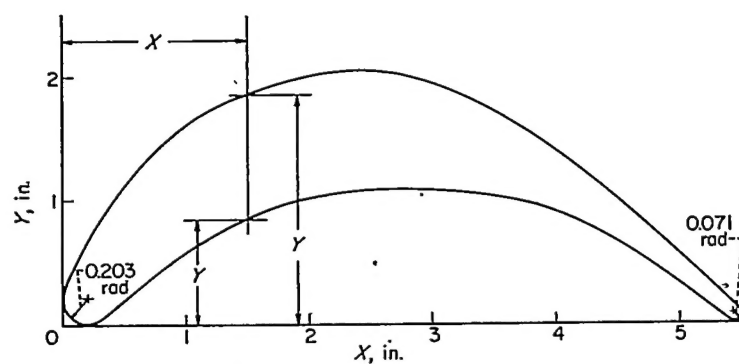
[90° impulse cascade; prescribed velocity distribution, fig. 5; incompressible flow]



$X$	$Y_{\frac{r}{2}}$	$Y_0$
0	0.203	0.203
.05	.069	.354
.10	.028	.466
.15	.009	.554
.20	.000	.647
.25	.006	.738
.30	.024	.821
.35	.061	.905
.40	.104	.985
.45	.147	1.063
.50	.189	1.135
.60	.272	1.253
.70	.353	1.352
.80	.430	1.440
.90	.504	1.520
1.0	.573	1.593
1.2	.701	1.718
1.4	.812	1.821
1.6	.899	1.904
1.8	.965	1.967
2.0	1.014	2.012
2.2	1.052	2.036
2.4	1.078	2.044
2.6	1.094	2.032
2.8	1.100	1.996
3.0	1.094	1.938
3.2	1.079	1.863
3.4	1.052	1.770
3.6	1.016	1.660
3.8	.969	1.536
4.0	.909	1.397
4.2	.831	1.246
4.4	.729	1.085
4.6	.608	.914
4.8	.473	.736
5.0	.325	.553
5.1	.248	.468
5.2	.167	.376
5.3	.085	.284
5.35	.044	.239
5.40	.007	.194
5.45	.003	.149
5.50	.071	.071

TABLE II.—STATIC TAP LOCATIONS ON BLADE SURFACE AT MIDSPAN

[90° impulse cascade]



Tap	X	Y	$\frac{x'}{c}$	$\frac{y'}{c}$	$\Phi$	$\Psi$	Tap	X	Y	$\frac{x'}{c}$	$\frac{y'}{c}$	$\Phi$	$\Psi$
9	0.015	0.280	-0.443	0.172	0	0	33	4.631	0.888	0.400	0.187	$\frac{26\pi}{16}$	0
10	.171	.595	-.412	.214	$\frac{\pi}{16}$		34	4.832	.709	.433	.161	$\frac{27\pi}{16}$	
11	.297	.816	-.385	.252	$\frac{2\pi}{16}$		35	5.038	.524	.467	.113	$\frac{28\pi}{16}$	
12	.418	1.014	-.360	.286	$\frac{3\pi}{16}$		36	5.248	.332	.502	.075	$\frac{29\pi}{16}$	
13	.535	1.180	-.336	.314	$\frac{4\pi}{16}$		37	5.468	.133	.538	.035	$\frac{30\pi}{16}$	
14	.668	1.321	-.309	.337	$\frac{5\pi}{16}$		38	5.384	.017	.621	.015	$\frac{31\pi}{16}$	
15	.817	1.454	-.280	.358	$\frac{6\pi}{16}$		39	5.147	.209	.481	.054	$\frac{32\pi}{16}$	
16	.974	1.575	-.249	.377	$\frac{7\pi}{16}$		40	4.871	.421	.435	.098	$\frac{33\pi}{16}$	
17	1.141	1.684	-.217	.394	$\frac{8\pi}{16}$		41	4.556	.635	.382	.142	$\frac{34\pi}{16}$	
18	1.314	1.780	-.184	.408	$\frac{9\pi}{16}$		42	4.369	.746	.350	.166	$\frac{35\pi}{16}$	
19	1.494	1.863	-.150	.420	$\frac{10\pi}{16}$		43	4.174	.842	.317	.187	$\frac{36\pi}{16}$	
20	1.873	1.985	-.079	.435	$\frac{12\pi}{16}$		44	3.960	.922	.279	.205	$\frac{37\pi}{16}$	
21	2.266	2.041	-.007	.438	$\frac{14\pi}{16}$		45	3.740	.984	.241	.220	$\frac{38\pi}{16}$	
22	2.464	2.042	.029	.435	$\frac{15\pi}{16}$		46	3.304	1.066	.163	.248	$\frac{39\pi}{16}$	
23	2.661	2.023	.064	.428	$\frac{16\pi}{16}$		47	2.859	1.099	.083	.257	$\frac{40\pi}{16}$	
24	2.857	1.981	.099	.417	$\frac{17\pi}{16}$		48	2.414	1.079	.002	.261	$\frac{41\pi}{16}$	
25	3.055	1.919	.134	.402	$\frac{18\pi}{16}$		49	1.975	1.008	-.078	.256	$\frac{42\pi}{16}$	
26	3.253	1.840	.168	.384	$\frac{19\pi}{16}$		50	1.764	.951	-.119	.250	$\frac{43\pi}{16}$	
27	3.451	1.744	.202	.363	$\frac{20\pi}{16}$		51	1.538	.875	-.160	.240	$\frac{44\pi}{16}$	
28	3.648	1.632	.236	.339	$\frac{21\pi}{16}$		52	1.342	.782	-.197	.227	$\frac{45\pi}{16}$	
29	3.844	1.507	.269	.313	$\frac{22\pi}{16}$		53	1.154	.673	-.233	.211	$\frac{46\pi}{16}$	
30	4.039	1.368	.302	.284	$\frac{23\pi}{16}$		54	.878	.459	-.294	.178	$\frac{47\pi}{16}$	
31	4.235	1.218	.334	.254	$\frac{24\pi}{16}$		55	.565	.244	-.347	.144	$\frac{48\pi}{16}$	
32	4.432	1.058	.367	.221	$\frac{25\pi}{16}$		56	.333	.046	-.303	.112	$\frac{49\pi}{16}$	